







Spectral Calculations of 3D Radiation Magnetohydrodynamic Simulations of Super-Eddington Accretion onto a Stellar-mass Black Hole

Brianna S. Mills¹ , Shane W. Davis¹ , Yan-Fei Jiang (姜燕飞)² , and Matthew J. Middleton³ 

¹ Department of Astronomy, University of Virginia, 530 McCormick Road, Charlottesville, VA 22904, USA; bri@virginia.edu

² Center for Computational Astrophysics, Flatiron Institute, New York, NY 10010, USA

³ Department of Physics and Astronomy, University of Southampton, Highfield, Southampton SO17 1BJ, UK

Received 2023 April 16; revised 2024 July 10; accepted 2024 August 2; published 2024 October 10

Abstract

We use the Athena++ Monte Carlo (MC) radiation transfer module to postprocess simulation snapshots from nonrelativistic Athena++ radiation magnetohydrodynamic (RMHD) simulations. These simulations were run using a gray (frequency-integrated) approach but were also restarted and ran with a multigroup approach that accounts for Compton scattering with a Kompaneets operator. These simulations produced moderately super-Eddington accretion rates onto a $6.62 M_{\odot}$ black hole. Since we only achieve inflow equilibrium out to 20–25 gravitational radii, we focus on the hard X-ray emission. We provide a comparison between the MC and RMHD simulations, showing that the treatment of Compton scattering in the gray RMHD simulations underestimates the gas temperature in the funnel regions above and below the accretion disk. In contrast, the restarted multigroup snapshots provide a treatment for the radiation field that is more consistent with the MC calculations, and result in postprocessed spectra with harder X-ray emission compared to their gray snapshot counterparts. We characterize these MC postprocessed spectra using commonly employed phenomenological spectral fitting models. We also attempt to fit our MC spectra directly to observations of the ultraluminous X-ray source (ULX) NGC 1313 X-1, finding best-fit values that are competitive to phenomenological model fits, indicating that first principle models of super-Eddington accretion may adequately explain the observed hard X-ray spectra in some ULX sources.

Unified Astronomy Thesaurus concepts: [Radiative transfer simulations \(1967\)](#); [Ultraluminous x-ray sources \(2164\)](#); [Magnetohydrodynamical simulations \(1966\)](#); [Astrophysical black holes \(98\)](#); [Schwarzschild black holes \(1433\)](#); [Stellar mass black holes \(1611\)](#); [X-ray astronomy \(1810\)](#); [Astronomy data modeling \(1859\)](#)

1. Introduction

Ultraluminous X-ray sources (ULXs) are point-like, off-nuclear extragalactic objects observed to have X-ray luminosities comparable to or in excess of the critical Eddington luminosity $L_X \gtrsim 10^{39} \text{ erg s}^{-1}$ (assuming isotropic emission for a $10 M_{\odot}$ black hole; see King et al. 2023; Pinto & Walton 2023, for reviews of ULXs). The majority of ULXs are generally thought to be X-ray binary systems with super-Eddington rates of accretion onto a compact object, a stellar-mass $M \lesssim 30 M_{\odot}$ black hole (Poutanen et al. 2007; Middleton et al. 2015a) or neutron star (Skinner et al. 1982; Bachetti et al. 2014). Some fraction of ULXs may result from sub-Eddington accretion rates onto intermediate-mass black holes (IMBHs) of $M \gtrsim 100 M_{\odot}$ (Farrell et al. 2009; Mezcua et al. 2013; Brightman et al. 2016; Earnshaw 2016; Webb et al. 2017; Oskinova et al. 2019).

If ULXs are indeed IMBHs, their spectra are expected to resemble scaled-up versions of black hole X-ray binary (BHXB) spectra, showing cooler accretion disks as the black hole mass increases (e.g., Miller et al. 2004). Observations of ULXs typically show a soft, thermal X-ray component and a hard thermal component with a rollover below $\sim 10 \text{ keV}$ (Gladstone et al. 2009; Bachetti et al. 2014), the latter supporting the interpretation of super-Eddington accretion. Early models debated whether this hard X-ray emission originated from coronal emission from IMBHs (Miller et al. 2004) or Comptonized emission from super-Eddington

accretion (Socrates & Davis 2006; Gladstone et al. 2009). However, classically, one would expect the innermost regions to have a different spectral shape due to optical depth effects and anisotropy (Poutanen et al. 2007).

The physical processes underlying super-Eddington accretion are still a topic of active research and numerical simulations are used to evaluate existing models and mechanisms. The classical picture of an optically thick, geometrically thin accretion disk (e.g., Shakura & Sunyaev 1973) is often used to model BHXBs, but the assumption of a thin disk is not self-consistent when the accretion rate exceeds a fraction of the Eddington luminosity ($L/L_{\text{Edd}} \gtrsim 0.3$). For larger luminosities the disk aspect ratio (H/R , with H as the scale height and R the radius) is no longer small, as assumed in the model. Super-Eddington accretion is expected to deviate from the classical Shakura & Sunyaev (1973) thin disk approximation, as the radiation pressure exceeds gravity. Processes like advection (Abramowicz et al. 1988) and radiatively driven outflows (Shakura & Sunyaev 1973; Ohsuga & Mineshige 2011) may reduce the radiative efficiency and result in geometrically thicker flows in the super-Eddington regime. Advection can directly affect the observed spectra (Straub et al. 2011; Kubota & Done 2019). Strong optically thick winds are also expected to be launched in these systems (and widely detected in ULXs: Middleton et al. 2014, 2015b; Pinto et al. 2016, 2020; Walton et al. 2016; Kosec et al. 2021), which likely shroud the outer accretion disk and can contribute additional low-energy flux for preferential sight lines.

Due to the complex nature of describing three-dimensional super-Eddington accretion flows, numerical simulations are a key tool for studying this regime. Several radiation



Original content from this work may be used under the terms of the [Creative Commons Attribution 4.0 licence](#). Any further distribution of this work must maintain attribution to the author(s) and the title of the work, journal citation and DOI.

hydrodynamic (RHD; Ohsuga et al. 2005), radiation magneto-hydrodynamic (RMHD; Ohsuga & Mineshige 2011; Jiang et al. 2014), and general relativistic RMHD (GRRMHD; Fragile et al. 2014; McKinney et al. 2014; Sądowski et al. 2015; Sądowski & Narayan 2016) simulations have been performed to understand the physical mechanisms involved in super-Eddington accretion. In these simulations, the radiation transfer equation is often integrated over frequency (the “gray” approximation) to reduce the computational expense. In many cases, the angle-integrated radiation moments (e.g., radiation flux and/or energy density) are solved for, which usually requires a closure relation (e.g., flux limited diffusion: Turner & Stone 2001; Howell & Greenough 2003; Krumholz et al. 2007; Moens et al. 2022; M1 closure: Levermore 1984; González et al. 2007; Skinner & Ostriker 2013; Wibking & Krumholz 2022; or the variable Eddington tensor method: Davis et al. 2012; Jiang et al. 2013, 2014; Asahina et al. 2020; Menon et al. 2022) to complete the radiation moments. An alternative approach, which is used for the simulations discussed in this work, is the direct solution of the gray radiation transfer equation (Stone et al. 1992; Jiang et al. 2014; Jiang 2021), which is then coupled to the fluid by computing the radiative cooling/heating and radiation force.

There have been significant efforts to simulate global accretion flows in the vicinity of black holes and utilize them to generate synthetic observables to compare with observations. Perhaps the most impactful is the effort by the Event Horizon Telescope to interpret the very long baseline interferometric images of M87* and Sgr A* (Event Horizon Telescope Collaboration et al. 2019, 2022). In these systems, the flows are relatively optically thin to electron scattering and the modeling of Compton scattering is not essential to this imaging effort. Our current study is focused on more radiatively efficient and optically thick flows where electron scattering opacity dominates. Previous work includes efforts to generate spectra from GRMHD simulations that utilized simple cooling prescriptions to keep the disk thin (Zhu et al. 2012; Schnittman et al. 2013; Kinch et al. 2019, 2021) to study the sub-Eddington or near Eddington regime, nonrelativistic RHDs simulations of super-Eddington accretion (Kawashima et al. 2012; Kitaki et al. 2017), and radiative GRRMHD simulations of the super-Eddington regime (Narayan et al. 2017).

Spectral postprocessing is commonly performed using Monte Carlo (MC) radiation transfer methods, which are useful for modeling the effects of Compton scattering. MC methods such as GRMONTY (Dolence et al. 2009), Pandurata (Schnittman et al. 2013), or RAIKOU (Kawashima et al. 2023) model Compton scattering and include general relativistic effects. The HEROIC code (Narayan et al. 2017) provides similar capabilities, but uses a combination of short and long characteristics instead of MC. These can also be coupled to photoionization calculations to produce predictions for atomic features, such as the Fe K α line (Kinch et al. 2019). The inclusion of Compton scattering is a key ingredient because it dominates the thermodynamic coupling between the radiation and gas near or above the photosphere (Narayan et al. 2017; Kinch et al. 2020).

In this work, we use the MC radiation transfer module in Athena++ to postprocess Athena++ RMHD simulation snapshots and aim to describe these results with current black hole accretion models, as well as compare the simulated spectra to data for the ULX NGC 1313 X-1. Although the simulations

performed here rely primarily on the nonrelativistic gray RMHD module, two recent developments to Athena++ offer potential improvements for future work. The first is a multigroup implementation (Jiang 2022) that facilitates multi-frequency transfer and better treatment of Compton heating and cooling. The second is a fully general relativistic formalism (White et al. 2023). As we discuss in Section 3.3, we utilize the multigroup method in this work to obtain a more accurate estimate for the temperature distribution in the current simulations. Spectral calculations with the GR implementation will be a focus of future work.

The plan of this work is as follows: In Section 2 we discuss the MC and Athena++ methods used in our spectral postprocessing analysis. In Section 3 we present the gray and multigroup RMHD spectral analysis results, along with image results and a comparison to phenomenological spectral models and fits to the spectrum of NGC 1313 X-1. We discuss the caveats, implications, and give a comparison of our results to previous work in Section 4. Finally, we summarize the key points of this work in Section 5.

2. Methods

We utilize the Athena++ code (White et al. 2016; Jiang et al. 2019; Stone et al. 2020) in two configurations—using the Athena++ RMHD simulation snapshots of super-Eddington accretion onto a $6.62 M_{\odot}$ black hole, and using the Athena++ MC radiative transfer module (S. W. Davis et al. 2024, in preparation) to postprocess the snapshots. Here we describe both configurations separately, and discuss the methods used for postprocessing in the last subsection.

2.1. Monte Carlo Radiation Transfer Code

The standard Athena++ RMHD simulations utilize gray opacities (frequency averaged opacities) and thus do not directly provide any spectral information. To extract frequency information needed to produce the spectra, we utilize the Athena++ MC radiation transfer module (Davis et al. 2009; S. W. Davis et al. 2024, in preparation) to compute the radiation field throughout an Athena++ simulation snapshot. The MC module utilizes the Athena++ code structure and mesh, allowing it to be run concurrently with the simulations. It can also be utilized to read in output simulation snapshot for postprocessing, which is how it is used here. Although the module can be used to perform MC transfer on the full three-dimensional refined simulation mesh, we focused here on two-dimensional axisymmetric calculations, where finer/coarser levels are prolonged/restricted to an intermediate refinement level uniform mesh. The MC calculation proceeds by creating and then tracking photon samples throughout the mesh. The samples (often referred to as photon packets or superphotons) can be viewed as statistical ensembles of a large number of photons with common properties. These properties of the photons are initialized and evolved using pseudorandom numbers to draw from distributions in positions, photon energies, scattering angles, etc., until they are either absorbed or leave the domain.

In this work we model free-free emission and absorption and unpolarized Compton scattering as the primary radiative processes. Each photon sample has a statistical weight corresponding to the number of photons in the packet. We model emission by randomly sampling each zone and assigning

a weight corresponding to the volume integrated free–free emissivity from the sampled cell. We assume a total number of photon samples N_s and N_{cell} cells in the mesh. If we label cells by index i and photons samples with index j , the total number of physical photons emitted in cell i can be written

$$N_i = \int \frac{j(\nu, T_i, \rho_i)}{h\nu} d\Omega d\nu \mathcal{V}_i \Delta t_{\text{int}}. \quad (1)$$

Here, Ω is the solid angle, \mathcal{V}_i is the volume of cell i , $j(\nu, T_i, \rho_i)$ is the free–free emissivity as function of temperature and density within the cell (Rybicki & Lightman 1979), and Δt_{int} is the (arbitrary) integration time interval. The statistical weights are defined so that

$$\sum_{j=1}^{N_s} w_j = \sum_{i=1}^{N_{\text{cell}}} N_i = N_{\text{ph}}, \quad (2)$$

where N_{ph} is the total number of physical photons emitted within the entire mesh. We can define the probability P_i for a photon to be emitted in zone i as $P_i = N_i/N_{\text{ph}} = 1/N_{\text{cell}}$. Then, the average number of photon samples emitted in cell i is $P_i N_s$, and we have

$$w_i = \frac{N_i N_{\text{cell}}}{N_s}. \quad (3)$$

This procedure yields photon weights that can differ by orders of magnitude. This is often frowned upon in the MC literature because more uniform weighting is generally variance reducing. We have, however, also implemented an equal weighting scheme where the initial cells of photon samples are chosen proportional to their volume-weighted emissivity and found this scheme ultimately results in larger statistical errors in our output spectra per computational second when compared with the scheme used here. This is primarily due to the large scattering optical depths to escape for photons launched in the highest emission cells (S. W. Davis et al. 2024, in preparation).

Finally, the direction of the photon is randomly sampled from an isotropic distribution, and the energy of the photon is drawn from a lognormal distribution in photon energy. We then further adjust the weights so that binned photons match the free–free distribution in photon frequency. Photon movement is handled in the Eulerian (coordinate) frame, while emission, scattering, and absorption occur in the comoving fluid frame. Photon sample properties are Lorentz boosted between the coordinate and fluid (comoving) frame for these interactions.

Photon samples are moved between scattering/absorption events by drawing an exponentially distributed dimensionless path length τ to the next absorption/scattering event via $\tau = -\ln \xi$, where ξ is a pseudorandom number uniformly distributed in the interval $[0, 1]$. This dimensionless path length can be thought of as the optical depth to the next scattering/absorption event, and is computed as a series of steps l_k (enumerated with subscript k) so that

$$\tau = \sum_k l_k(\alpha_{\nu,k} + \sigma_{\nu,k}), \quad (4)$$

where α_{ν} is the absorption extinction coefficient and σ_{ν} is the scattering extinction coefficient. The scattering and absorption coefficients are the products of the corresponding opacities and density, which are evaluated in the comoving frame and then boosted to the Eulerian frame. In the scheme used here each

step k represents a movement of the photon sample to the location of the next scattering/absorption event or the nearest cell face, whichever comes first. This continues until the requisite value of τ is reached or the photon sample escapes the domain. Photon samples are assumed to travel along straight lines, but we use a spherical mesh, so that computing where the photon sample leaves the current cell requires solving quadratic relations and accounting for possible turning points in r and θ (S. W. Davis et al. 2024, in preparation).

Each interaction of a photon sample with matter results in a combination of absorption and scattering, which is handled by reductions in w . We have $w' = w\epsilon$, where w' is the new weight after scattering and

$$\epsilon = \frac{\alpha_{\nu}}{\alpha_{\nu} + \sigma_{\nu}}. \quad (5)$$

If the statistical weight falls below a small threshold value (based on the initial emissivity), the photon is considered absorbed and further evolution is terminated. The outgoing photon energy and direction after Compton scattering follow from procedures described in Pozdnyakov et al. (1983), except that we tabulate the scattering cross section using a method similar to that described in Dolence et al. (2009).

When photons escape through the domain boundary, their energies, locations, and angles are tabulated in a photon list output that is then used to generate spectra. The MC calculation also tabulates cell-averaged radiation moments such as the energy density, radiation flux vector, and pressure tensor, as well as user-defined quantities such as the net radiative cooling, average photon energy, and average energy mean opacity in each cell. These are output in standard Athena++ formats, such as HDF5 and VTK.

2.2. Athena++ Radiation Magnetohydrodynamic Simulation Snapshots

Athena++ has been rewritten in C++ compared to its predecessor, Athena (Stone et al. 2008). Athena++ now includes adaptive mesh refinement (Stone et al. 2020) and special and general relativistic capabilities (White et al. 2016, 2023). In the current work, however, a pseudo-Newtonian potential is used to mimic the effects of general relativity around a Schwarzschild black hole (Paczynski & Wiita 1980). Results from a GRRMHD implementation of Athena++ and subsequent spectra will be reported in future work.

We performed a series of global, three-dimensional RMHD simulations of a $6.62 M_{\odot}$ black hole accreting at several super-Eddington mass accretion rates assuming a 10% radiative efficiency so that $\dot{M}_{\text{Edd}} \equiv 10L_{\text{Edd}}/c^2$. We used the explicit integration RMHD module in Athena++, which uses an algorithm similar to Jiang et al. (2014), but with updates that solve a radiation transfer equation of the form presented in Jiang (2021). The simulation setup for these snapshots is similar to the setup described in Huang et al. (2023), where the ideal MHD equations are coupled with the time-dependent radiation transfer equation (see Jiang et al. 2014, Equations (1)–(4); Jiang 2021, Equations (4)–(6)). A rotating gas torus was initialized in hydrostatic equilibrium and threaded with toroidal magnetic fields. Accretion onto the black hole happens via the magnetorotational instability (Balbus & Hawley 1991) and the mass accretion rate is varied for each simulation based

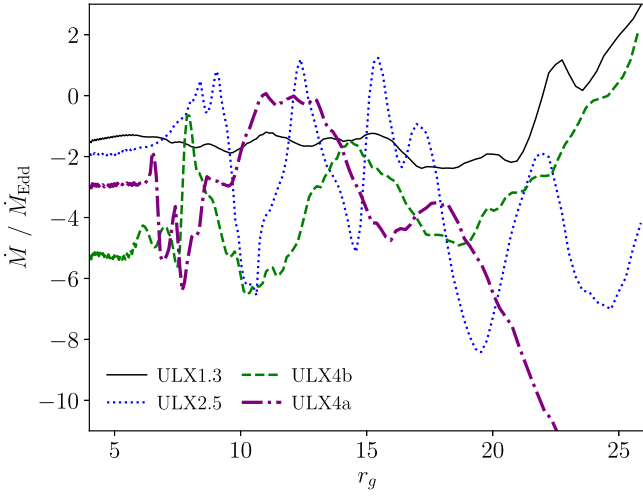


Figure 1. The mass accretion rate \dot{M} as a function of gravitational radius r_g from the black hole for each Athena++ RMHD simulation snapshot (see Table 1). ULX4a is the purple dotted–dashed line, ULX4b is the green dashed line, ULX2.5 is the blue dotted line, and ULX1.3 is the black solid line.

on the initial magnetic field configuration (see, e.g., Huang et al. 2023).

The simulations self-consistently form an accretion disk and reach a quasi-steady state for the inner disk. Figure 1 shows the mass accretion rate in terms of \dot{M}_{Edd} for a $6.62 M_{\odot}$ black hole as a function of radius within the inner $25 r_g$ where $r_g = GM/c^2$ is the gravitational radius. The mass accretion rates are relatively steady state within $25 r_g$ of the black hole, but not at larger radii. The four snapshots and their radially averaged mass accretion rates (over the $25 r_g$) are listed in Table 1. Snapshots ULX4a and ULX4b have nearly the same mass accretion rate ($\dot{M} \simeq -4\dot{M}_{\text{Edd}}$) and are both from the same simulation run (at different times), thus we named them ULX4a and ULX4b. Snapshot ULX2.5 and snapshot ULX1.3 are independent simulation runs with average mass accretion rates of $\dot{M} \simeq -2.5$ and $-1.3\dot{M}_{\text{Edd}}$, respectively.

Although the Athena++ RMHD calculations have adaptive mesh refinement capabilities, the MC code works most efficiently on a uniform grid. For efficient parallelization, we chose one uniform refinement level for our analysis. We selected an appropriate refinement level such that all snapshot grids were approximately the same size $256 \times 128 \times 256$ cells in r , θ , and ϕ (respectively). The accretion disk located in the inner $25 r_g$ roughly corresponds to the 80 innermost zones in radius at this level, and covers a range of θ from 0 to π , and a range of ϕ from 0 to 2π . Due to the approximately axisymmetric nature of the simulations, we chose to azimuthally average each snapshot for our postprocessing analysis. This has little effect on the output spectra, but greatly improves the statistics for cell-averaged quantities, examples of which are presented in Figures 3–6.

Figure 2 shows the gas density in snapshot ULX2.5 for the inner $25 r_g$ where the accretion disk has roughly reached inflow equilibrium, and the small inset plot shows the full simulation grid out to $500 r_g$. The full simulation grid includes the geometrically thick gas torus extending from $\sim 100 r_g$ to $\sim 300 r_g$. The densities in the funnel regions are several orders of magnitude lower than the densities in the optically thick accretion disk and gas torus. We discuss the implications of the low-density funnel region and the impact of the torus geometry in Section 3.1.

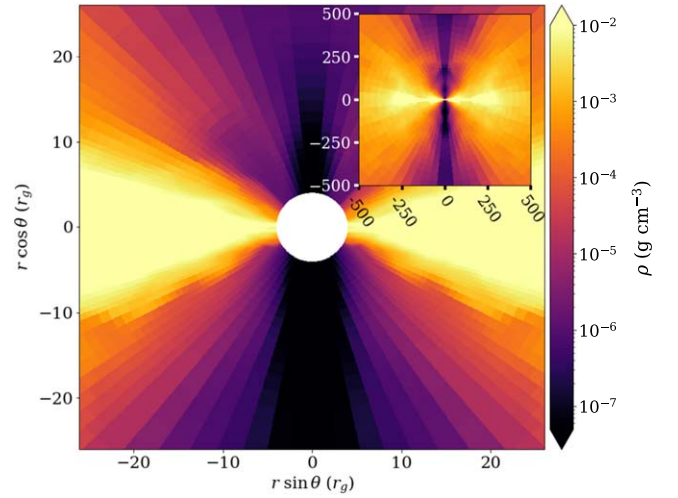


Figure 2. Azimuthally averaged gas density ρ (units of g cm^{-3}) of Athena++ RMHD simulation snapshot ULX2.5 showing the inner $25 r_g$ with a small inset plot showing the gas density out to $500 r_g$.

Table 1
Athena++ Radiation Magnetohydrodynamic Simulation Snapshots

Snapshot	$\langle \dot{M} \rangle / \dot{M}_{\text{Edd}}$	θ_f	L_f ($\text{erg cm}^{-2} \text{s}^{-1}$)	η_f
ULX4a	-4.15	37°	1.03×10^{39}	2.56%
ULX4b	-3.93	37°	8.77×10^{38}	2.29%
ULX2.5	-2.53	50°	2.78×10^{38}	1.13%
ULX1.3	-1.31	55°	1.51×10^{38}	1.18%
ULX4a-MG	-4.02	37°	1.31×10^{39}	3.34%
ULX2.5-MG	-2.53	50°	4.73×10^{38}	1.92%

Note. Athena++ RMHD simulation snapshots of a $6.62 M_{\odot}$ black hole used in this analysis. All snapshots are azimuthally averaged and are limited to the inner $25 r_g$. The first column corresponds to the ratio of the radially averaged mass accretion rate (\dot{M}) in terms of the Eddington mass accretion rate \dot{M}_{Edd} . The negative sign indicates accretion toward the black hole. The second column corresponds to the polar funnel angle θ_f , the opening angle relative to the polar axis representing the approximate boundary between the funnel region and the accretion disk. Photons emerging from this polar funnel angle are collected for spectral postprocessing and have corresponding funnel luminosity L_f . The last column is the calculated radiative efficiency η_f of the funnel region. Snapshots ULX4a and ULX4b were taken from the same simulation run (at different times), whereas snapshots ULX2.5 and ULX1.3 are independent simulation runs. The snapshots with the suffix “-MG” correspond to the two gray simulations chosen for the multigroup RMHD implementation (Jiang 2022).

The net cooling in the Athena++ RMHD simulations is given by

$$\dot{C} = c\rho(\kappa_P a T_g^4 - \kappa_E E_r) + c\rho\kappa_{\text{es}} \frac{4kT_g - \langle h\nu \rangle}{m_e c^2} E_r, \quad (6)$$

where c is the speed of light, ρ is the gas density, κ_P is the Planck mean opacity, a is the Planck temperature constant, T_g is the gas temperature, κ_E is the energy mean opacity, E_r is the radiation energy density, κ_{es} is the electron scattering opacity, k is the Boltzmann constant, h is the Planck constant, $\langle h\nu \rangle$ is the average photon energy, and m_e is the electron mass. The first term is the frequency- and angle-integrated free–free emissivity $\eta_{\text{ff}} = c\rho\kappa_P a T_g^4$. The second term is the heating term associated with absorption, and the last term is the net Compton cooling.

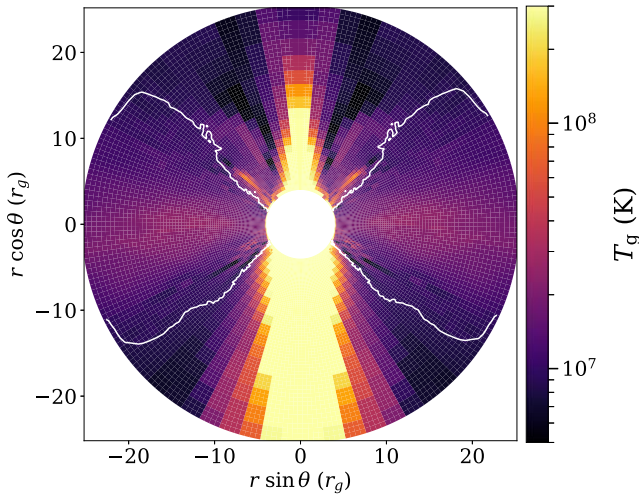


Figure 3. Gas temperature T_g (K) shown for snapshot ULX2.5. The white contour line corresponds to $F_r/cE_r = 0.3$, which is roughly equivalent to the effective photosphere boundary and defines the polar funnel angle $\theta_f = 50^\circ$ from the polar axis. The apparent asymmetry of the gas temperature in the funnel regions above and below the disk is a result of this particular simulation taken at this moment in time. The temperatures were capped at a maximum of 3×10^8 K and a minimum of 10^6 K.

In the RMHD simulations, the radiation field is assumed to be a blackbody so $\langle h\nu \rangle = 4kT_r$, where T_r is the radiation temperature $T_r = (E_r/a)^{1/4}$. The simulations also assume that $\kappa_E = \kappa_p$. These assumptions and their impact on the gas temperature distribution and the spectra that result will be discussed further in Section 3.

The gas temperature of the same snapshot in Figure 2 is shown in Figure 3. Note that the apparent asymmetry of the gas temperature in the funnel regions above and below the disk is due to the randomness in the flow at the time this snapshot was taken. Prior to postprocessing, we set a lower limit on the gas temperature of 10^6 K and an upper limit of 3×10^8 K (except for the multigroup snapshots, which we set the upper limit to 10^9 K). The gas temperature is hottest in the funnel region where it hits the temperature cap of 3×10^8 K, and the gas in the accretion disk peaks at a few $\times 10^7$ K. Although the temperatures in the funnel regions are large, the corresponding gas densities from Figure 2 are small (10^{-8} g cm $^{-2}$) so the optical depth to scattering is extremely low and the contribution to the emission from the hottest simulation cells is relatively weak. The white contour lines roughly define the effective photosphere boundary between the accretion disk and the funnel region, defined by $F_r/cE_r = 0.3$, where F_r is the $r\phi$ component of the radiative flux and E_r is the radiation energy density. This flux ratio is consistent with methods that define the photosphere by integrating to an optical depth $\tau = 1$ surface (Chandrasekhar 1960; Kinch et al. 2019). The polar angle of this boundary is used to approximate the funnel opening angle θ_f , which is then used to calculate the luminosity, spectra, and images in Section 3.2.

2.3. Spectral Postprocessing

Here we describe the methods used for performing our spectral analysis. Spectra were generated for each azimuthally averaged snapshot, truncating the calculation to only model MC transfer within $25 r_g$. The properties of all photon samples leaving the domain at $25 r_g$ are tabulated in a list, which is then

used to generate spectra. This truncation radius was chosen primarily because the outer disk radii are not yet in steady state. In particular, the initial torus is thick, which requires an extremely large radiation pressure. Hence, this torus is not in thermal equilibrium, and is rapidly cooling. We then ran the MC code on a copy of each snapshot grid, initializing 10^7 photons for snapshots ULX4a and ULX4b, and about 10^8 photons for the other two snapshots. The reason for the difference is due to the larger optical depths and mass accretion rates in ULX4a and ULX4b that result in a factor of ~ 10 difference in number of scatterings per photon sample. Recall that the number of scatterings per photon sample is proportional to the square of the optical depth. Increasing the number of photons in the MC calculations greatly improves the counting statistics, however we found that more than 10^7 photons for those snapshots became too computationally expensive due to the large scattering optical depths.

Photons that escaped the $25 r_g$ simulation domain were collected and distributed into 64 photon energy bins ranging from 0.1 to 60 keV, and eight direction angles. By direction angle, we mean the angle θ_p that the photon momentum vector makes with the polar axis. We use the subscript p to distinguish angles related to the photon momentum from those related to spherical polar coordinate angles. For example

$$\theta_p = \arccos\left(\frac{\mathbf{p} \cdot \hat{\mathbf{z}}}{|\mathbf{p}|}\right), \quad (7)$$

where \mathbf{p} is the photon momentum vector. These angle bins are distributed uniformly in $\cos \theta_p$ and integrated over azimuthal direction angle ϕ_p . When binning, we do not distinguish between photons leaving above or below the disk. For example, photons with $\theta_p \sim 0$ will be placed in the same bin as photons with $\theta_p \sim \pi$.

We select only photons which escape through a “funnel-like” region above and below the disk. Specifically, we only bin photons within a coordinate opening angle of θ_f from the polar axes, retaining photons leaving the domain at $\theta < \theta_f$ or $\theta > \frac{\pi}{2} - \theta_f$. This excludes photon samples that leave domain closer to the midplane. Such photons would almost certainly be further scattered in the optically thick accretion disk if we extended our domain outwards. Hence, we select our funnel opening angle θ_f to roughly correspond to the location of the disk photosphere at $25 r_g$. The approximate values for this funnel opening angle are listed for each snapshot in Table 1.

Due to these selections, the resulting spectra are only expected to be useful estimates of the hard X-ray emission as the softer X-rays will have a significant contribution from regions with $r > 25 r_g$. We also cannot infer much about the angular distribution of the escaping photons for angles that are more edge on than θ_f as such photons would likely interact with an optically thick flow beyond $r = 25 r_g$.

In the case of snapshot ULX2.5 we also perform an MC calculation using the full simulation domain. In this case we collect all photon samples leaving the domain, but find that the spectrum of the escaping radiation is dominated by contributions from the torus. Due to large optical depths in the outer torus, the calculation is computationally expensive and run with fewer photons, yielding a lower signal-to-noise ratio spectrum. For these reasons, we do not report spectra from these runs, but we do use the cell-averaged radiation outputs for comparison with the truncated runs described above.

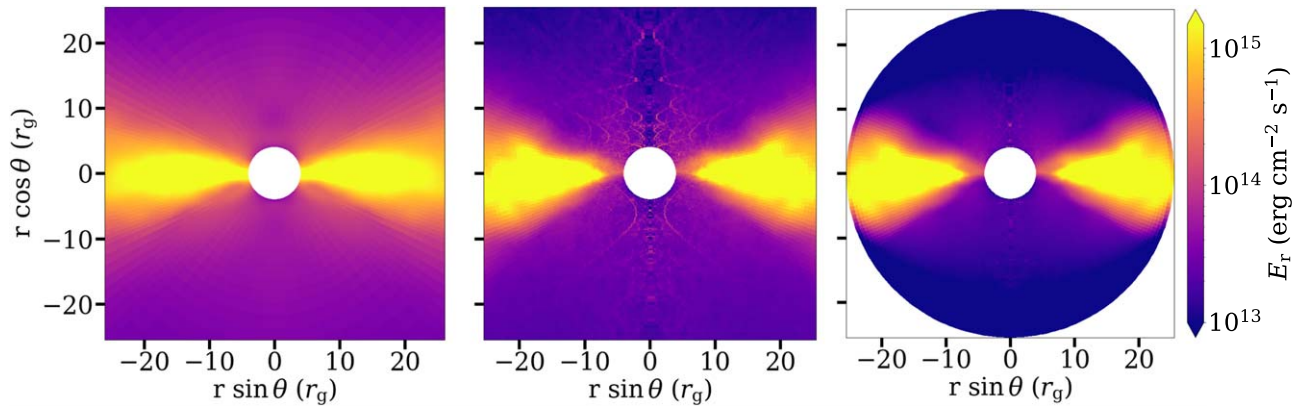


Figure 4. Azimuthally averaged radiation energy density of snapshot ULX2.5 for the *Athena++* RMHD simulation (left panel), the MC calculation (middle panel), and the MC calculation with the simulation grid truncated at $r = 25 r_g$ (right panel). In the left and middle panels, only the inner $25 r_g$ are plotted here for comparison, but the full simulation grids extend out to $500 r_g$.

3. Results

3.1. Comparing *Athena++* with Monte Carlo

We first compare cell-averaged quantities. Figure 4 shows a comparison of E_r computed with MC to the azimuthally averaged E_r from the *Athena++* simulation snapshot. This figure is for snapshot ULX2.5, but the result is representative of all four snapshots in this analysis. The RMHD simulation result is plotted in the left panel, and two MC calculations are plotted in the middle and right panels, respectively. The middle panel shows the results of an MC calculation using the full simulation domain out to $\sim 500 r_g$, whereas the right panel shows the MC calculation when the grid is truncated at $25 r_g$. The two MC calculations show precise agreement in the accretion disk, where the radiation field is nearly in radiative equilibrium with the gas. They also agree reasonably well in the funnel regions, deviating by only a small factor near the outer edge of the truncated domain. This suggests that the E_r in the inner $25 r_g$ is dominated by the locally emitted radiation field, since the truncated calculations have no incoming photons on the boundary. Therefore, the radiation from the cooling torus, which dominates the overall emission in the full domain calculation, is not providing a significant contribution in the inner disk region. Our comparison suggests that radiation outside the truncated domain is contributing $\lesssim 30\%$ near $25 r_g$, and $\lesssim 15\%$ near the photosphere boundary of the disk.

Note that at the very edge of the truncation boundary, E_r is slightly lower compared to the radiation energy density in the full domain calculation, as the truncated calculation assumes no incoming radiation flux. The more noticeable streaks of high E_r noise in the funnel regions in the MC full domain calculation are attributed to the factor of 10 fewer photons used to compute the full grid, resulting in a larger statistical variance.

Comparing the gray RMHD module E_r to the MC calculations in Figure 4, they also appear to agree within a factor of order unity in the accretion disk midplane, but start to deviate more significantly as one transitions into the funnel region. In the funnel, this deviation is as much as a factor of 10. The MC calculations find a significantly lower E_r in the funnel region. This mismatch is even more evident in Figure 5, which shows the ratio of the two calculated energy quantities: the mean photon energy $\langle h\nu \rangle$ calculated by the truncated MC calculation, and the mean photon energy $4kT_r$ assumed in the *Athena++* RMHD module. The dark regions where the ratio

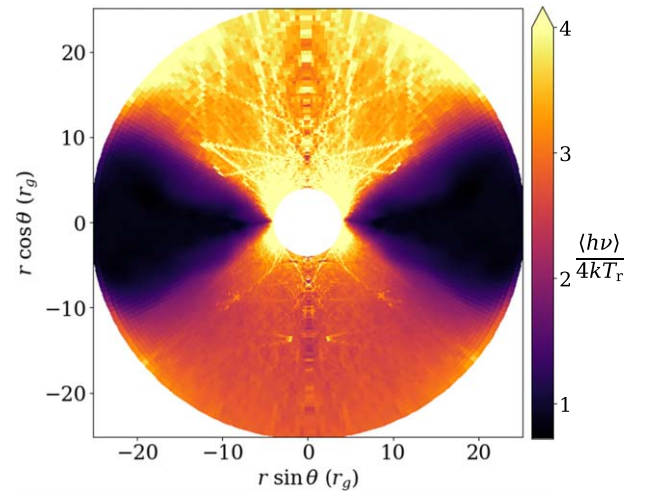


Figure 5. Ratio of the mean photon radiation energy $\langle h\nu \rangle$ calculated in the MC code and the radiation energy $4kT_r$ in the RMHD simulation for snapshot ULX2.5 where T_r is the radiation temperature (assuming the blackbody approximation). The streaks in the funnel region are artifacts of low photon statistics in the MC calculation.

is of order unity show that the MC and *Athena++* generally agree in the accretion disk, but deviate in the funnel region above and below the disk. In these regions, the MC calculates that average photon energy is at least 3 times higher than assumed in the RMHD run. The assumption that the radiation field is approximately blackbody works well for the optically thick accretion disk regions, but is inadequate in the optically thin funnel regions.

In Figure 6, we compare the resulting cooling computed by the *Athena++* RMHD simulation (left panel) to the same term evaluated by the MC calculation (right panel) for the same snapshot. The net cooling is calculated using Equation (6) where positive values indicate cooling and negative values indicate heating. Since the Compton cooling is the dominant term in Equation (6) within the funnel region, this comparison is strongly dependent on the degree to which $\langle h\nu \rangle$ differs from $4kT_r$ and the ratio of E_r in the MC calculations relative to RMHD (see Figures 4 and 5). We find that the cooling calculated by the MC code deviates significantly from that of the RMHD simulation, particularly in the funnel regions, where the MC code shows significantly more heating and less cooling. In the accretion disk, the MC code provides slightly

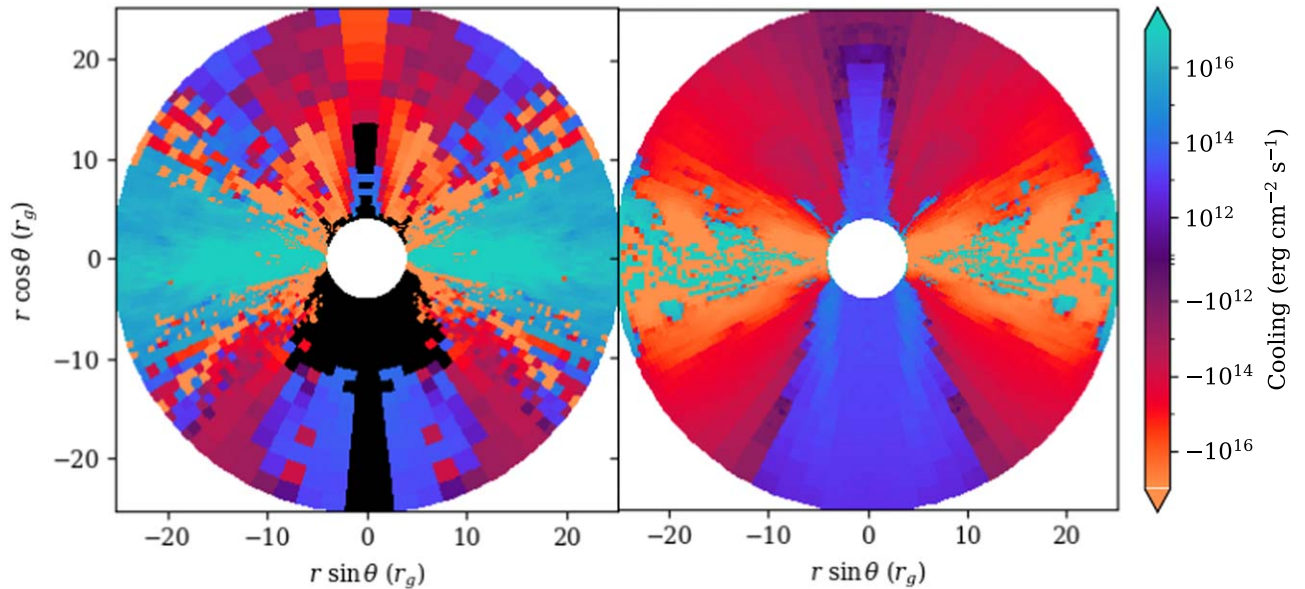


Figure 6. Comparison of the net cooling of snapshot ULX2.5 in the Athena++ RMHD simulation (left panel) and the MC 25 r_g calculation (right panel). The snapshot has been azimuthally averaged in both cases. The net cooling is given by Equation (6) where positive values signify net cooling and negative values imply net heating. The black cells extending into the photosphere in the RMHD calculation are artifacts of this particular moment in the simulation.

less cooling than the RMHD simulation does. The amplitude of the cooling is large in this region because E_r is large. Even though the disk is optically thick, it is hot enough that the Compton term dominates over free-free emission and absorption in both the RMHD and MC calculations. Since $\langle h\nu \rangle \simeq 4kT_g$ to within a few percent, even small statistical noise in the MC calculation will cause either a large net heating or cooling term here. Hence, most of the fluctuation seen in the MC calculation in the disk is due to noise in the MC calculation.

These results suggest that if the RMHD simulations had a better estimate for $\langle h\nu \rangle$ it would be higher than $4kT_r$. In an approximate steady state with the Compton cooling term dominating in the funnel region, one expects $\langle h\nu \rangle \simeq 4kT_g$. By underestimating $\langle h\nu \rangle$, the RMHD simulations tend to underestimate T_g in the optically thin regions above the disk and near the photosphere. This underestimate also tends to increase T_r to better balance T_g , causing the RMHD simulations to overestimate E_r , consistent with our findings above. This also means that spectra computed from these snapshots will have lower average photon energies than one might obtain in a simulation with more self-consistent thermodynamics, which would yield higher T_g and harder X-ray spectra. We explore the implications of this in Section 3.3.

3.2. Postprocessed Spectra and Compton Cooling from Gray Radiation Magnetohydrodynamic Simulations

We present postprocessed X-ray spectra for the four gray RMHD snapshots in Figure 7. For the lower- \dot{M} snapshots (ULX1.3 and ULX2.5), the spectral peaks are roughly around 5 keV, whereas the higher- \dot{M} snapshots (ULX4a and ULX4b) have peaks that are shifted slightly to around 7 keV. The hard X-ray tails appear to follow power laws, which we characterize with XSPEC (Arnaud 1996) model fits in Section 3.4. Due to the truncation of the simulation grids at 25 r_g prior to postprocessing, the softer X-ray emission that should be coming from larger radii is largely absent in these spectra so only the hard X-ray are self-consistently modeled.

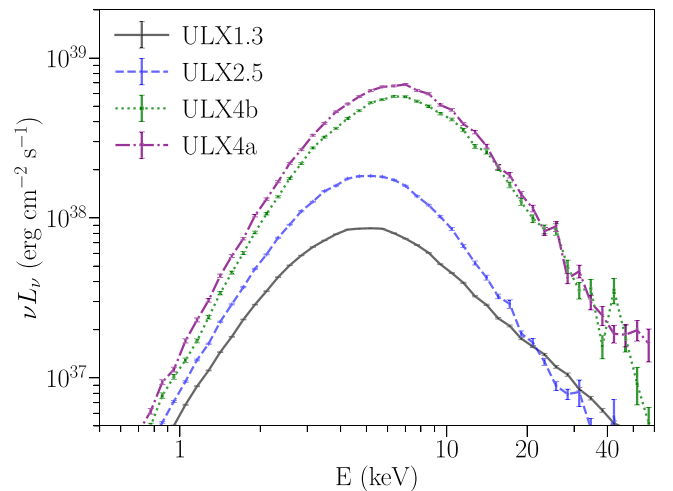


Figure 7. MC postprocessed X-ray spectra from the gray RMHD simulation snapshots. From top to bottom: ULX4a (magenta dashed-dotted line), ULX4b (green dotted line), ULX2.5 (blue dashed line), and ULX1.3 (black solid line). Snapshots ULX4a and ULX4b were taken from the same simulation run, while ULX2.5 and ULX1.3 are both from independent simulations. Note that these spectra only include the inner 25 r_g emission escaping out through a polar funnel angle θ_f specified in Table 1 for each snapshot.

The frequency-integrated luminosities for each spectrum are tabulated in Table 1. We label these funnel luminosities L_f to emphasize that we only tabulate the contributions from photons leaving the domain at coordinate θ within an angle θ_f of the polar axes. Note that these are mostly hard X-ray luminosities due to the missing soft emission from the outer disk. The contour lines in Figure 3 approximate the funnel opening angle for ULX2.5 ($\theta_f = 50^\circ$), which we show as a representative snapshot. The θ_f and corresponding funnel luminosities L_f are listed for each snapshot in Table 1.

Photons emerging closer to the disk midplane than θ_f are excluded because their escape from the truncated domain at $r = 25 r_g$ is largely artificial. If we had instead extended our MC calculation domain outward in radius, these photons would

likely experience additional scattering and absorption in the optical thick flow before escaping. Slight variations in θ_f can have a modest effect on the funnel luminosity and the resulting spectral shape. For example, in the case of ULX2.5 the funnel luminosity varied by less than 17% when varying θ_f by $\pm 10^\circ$. Choosing a narrower funnel angle ($\theta_f = 40^\circ$) gave a luminosity of $L_f = 2.04 \times 10^{38} \text{ erg s}^{-1}$, whereas choosing a wider funnel ($\theta_f = 60^\circ$) gave a slightly higher luminosity of $L_f = 3.36 \times 10^{38} \text{ erg s}^{-1}$. The spectral shape did not change when θ_f decreased (inside the funnel region). Increasing θ_f , however, results in a slight softening of the spectrum as there is an increase in the flux of photons escaping below what would be the photosphere in a more extended domain. These photons tend to be softer because they are emitted from the cooler regions of the disk. We found this to be true for all snapshot spectra in this analysis.

The radiative efficiency calculated for Snapshot ULX2.5 is $\eta_f = 1.51\%$ for a nominal mass accretion rate of $-2.53\dot{M}_{\text{Edd}}$ ⁴. We report the calculated radiative efficiency in the funnel η_f for each snapshot in Table 1. Generally for super-Eddington accretion, it is expected that the radiative efficiency will be lower than the $\sim 5\% - 10\%$ inferred for thin disks, decreasing as accretion rate increases. We do generally find lower efficiencies, but the results are not completely consistent with expectations. Comparing the efficiencies between snapshots ULX2.5 and ULX1.3, which have similar θ_f , we infer a slightly lower efficiency as accretion rate increases. Snapshots ULX4a and ULX4b, have a higher \dot{M} than the other snapshots, but also show a higher η_f . This would imply that the accreted material is moving faster in the lower accretion rate runs.

It is also possible that part of this deviation from the expected trend is a result of our truncation of the calculation at $r = 25 r_g$ and merits more consideration in future work exploring a wider range of \dot{M} . We also note that the efficiencies quoted here may be as much as a factor of ~ 2 too low, as they only include emission from the funnel region within $25 r_g$. Thus, the funnel efficiencies η_f reported in Table 1 serve as lower limits in this analysis.

We also examine the angular distribution of the emission, which we model as the flux fraction (ratio of the specific intensity I to the flux F) for each spectrum in Figure 8. For observations, this should roughly correspond to the inclination viewing angle dependence with respect to the polar axis. A face-on view of the emission corresponds to $\cos \theta_p = 1$, and an edge-on view corresponds to $\cos \theta_p = 0$. Snapshot ULX1.3 is shown as the solid black line, ULX2.5 is the dashed blue line, ULX4b is the dotted green line, and ULX4a is the dashed-dotted pink line. The flux fraction has been integrated over all frequencies ν for improved statistics, so the resulting distribution is most representative of the angular distribution near the spectral peak.

Although we show the full distribution for $\cos \theta_p$ ranging from 0 to 1, we emphasize that the $\cos \theta_f$ ranges from 0.57 for ULX1.3 to 0.8 for snapshots ULX4a and ULX4b. Hence, only bins with $\cos \theta_p$ greater than these values are likely to be well characterized. Over this limited range, the angular distributions are relatively flat, but notably do not peak at the most face-on inclination bin. This is contrary to standard expectations where a face-on view provides the largest projected area and, thus, the largest flux. As θ_p approaches the edge-on view the intensity declines by factors of several. However, we emphasize that the

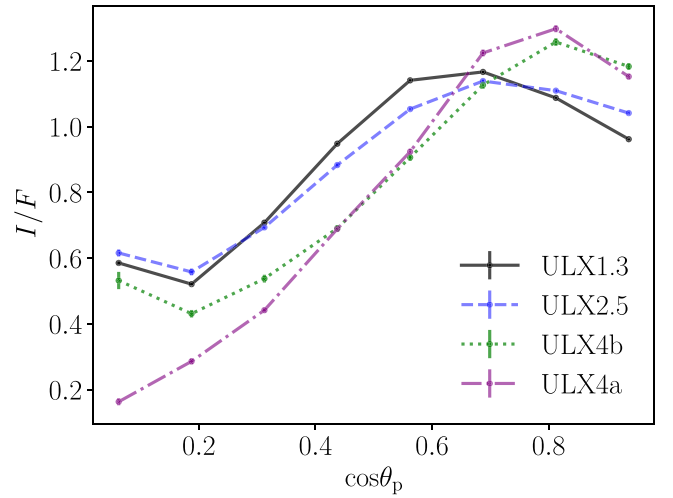


Figure 8. Limb darkening (flux fraction of the specific intensity I to the isotropic flux F) as a function of inclination angle in terms of $\cos \theta$ for snapshots ULX4a (pink dashed-dotted line), ULX4b (green dotted line), ULX2.5 (blue dashed line), and ULX1.3 (black solid line). Note that each snapshot spectrum was generated using only photons which escape through a funnel opening of polar angle θ_f specified in Table 1. Face-on viewing corresponds to $\cos \theta_p = 1$ and edge-on viewing corresponds to $\cos \theta_p = 0$.

intensity distribution at these angles will undoubtedly be impacted by the extension of the optically thick disk outside of the calculations domain. For example, the slight rise in the most edge-on bin is almost certainly a result of our artificial truncation of the simulation domain. Hence, our current results cannot provide reliable predictions about geometric beaming factors.

To better interpret these results, we show a set of reconstructed images in Figure 9, which shows the frequency-integrated intensity from the funnel region at different inclination angles $\theta_p \sim 49^\circ$ (left column; funnel edge view) and $\theta_p = 0^\circ$ (right column; face-on view) for two snapshots: the gray RMHD snapshot ULX2.5 (top row), and the multi-group RMHD snapshot ULX2.5-MG (bottom row). We discuss the latter snapshot in detail in the next section. The corresponding opening angle for both snapshots is $\theta_f = 50^\circ$. Photons escaping the funnel were extrapolated out to a distance of $\sim 250,000 r_g$ to form these images. In the face-on case, we see a deficit for photons near the polar axis, along the line of sight to the black hole. In this region the densities are so low that relatively few photons are scattered or emitted toward the observer. Near the edge of the funnel, the intensity of the emission appears to brighten compared to the face-on inclination. This enhancement is consistent with modest amounts of relativistic beaming in the mildly relativistic outflowing gas. This beaming is largest at these moderate inclinations where both the line-of-sight outflow velocities and scattering optical depths are large.

3.3. A Multigroup Radiation Magnetohydrodynamic Approach

As discussed in Section 3.1, the $\langle h\nu \rangle = 4kT_r$ assumption in the gray RMHD simulations likely results in gas temperatures being underestimated in the regions above the optically thick disk. This, in turn, means that the MC spectra we compute are probably softer than they should be if the temperatures were computed with a more self-consistent treatment of Compton scattering. In an effort to recompute the gas temperature, we first tried to use the MC code to calculate the net cooling everywhere in the simulation and balanced this with dissipation

⁴ We define \dot{M}_{Edd} assuming 10% efficiency, but \dot{M} itself is independent of our assumed efficiency.

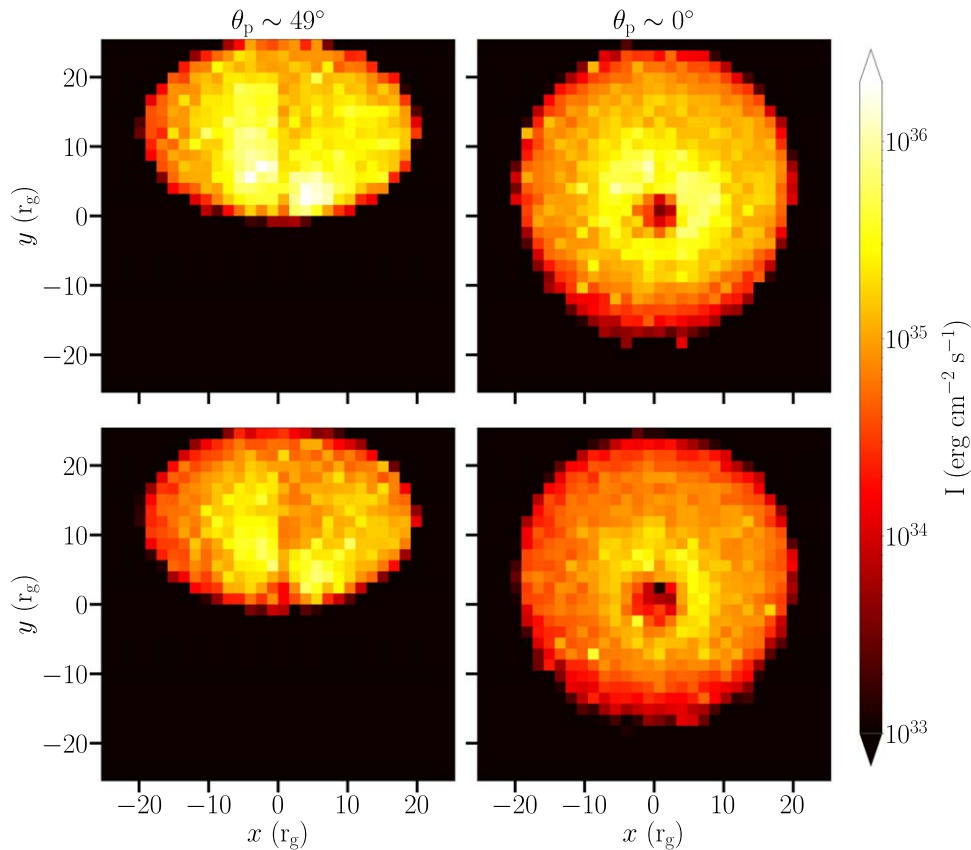


Figure 9. A series of frequency-integrated images showing the emergent radiation intensity for snapshots ULX2.5-MG (top row) and ULX2.5 (bottom row) for two inclination viewing angles. The left column shows a viewpoint from an inclination of $\theta_p \sim 49^\circ$, which is at the edge of the funnel for these snapshots ($\theta_f = 50^\circ$). The right column views a face-on inclination ($\theta_f = 0^\circ$). The photons leaving the simulation domain at $25 r_g$ were extrapolated out to a distance of $250,000 r_g$ from the black hole.

from the RMHD snapshots. We found, however, that the recomputed temperatures in the funnel had too large of a variance due to the limited photon statistics, and did not consistently converge after several iterations.

Instead, we utilized the multigroup radiation module described in Jiang (2022), which extends the gray radiation scheme in Jiang (2021) to include frequency dependence and treats Compton scattering using a Kompaneets-like approximation for the electron scattering source term. We used 20 logarithmically distributed frequency groups to cover the frequency space over 3 orders of magnitude, which increased the computational cost by a similar factor. Hence, a full three-dimensional simulation with this method would be extremely computationally expensive. Here, we instead begin the multigroup simulation by assuming the initial spectrum to be a blackbody, and thus restart the gray simulation and run for a time just long enough for the gas above the disk to reach a new temperature equilibrium. This makes the computational expense feasible for this study because the thermal timescale in the funnel region is very short.

We performed the multigroup procedure for two of the four snapshots, ULX2.5 and ULX4a, using the restart files from the gray RMHD simulations and running them with 20 frequency groups. We label the new snapshots from these multigroup runs ULX2.5-MG and ULX4a-MG. These snapshots were computed at approximately the same time as their gray counterparts, and thus have the same average mass accretion rates (see Table 1) and the density distributions are quite similar. However, as expected from the MC calculations of cooling

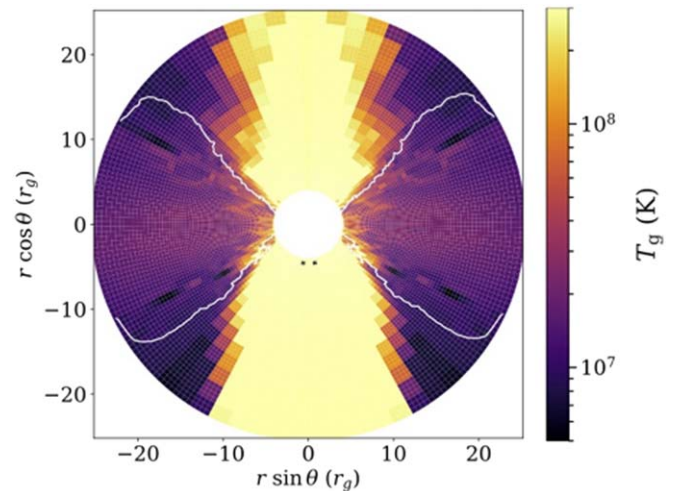


Figure 10. Gas temperature T_g (K) shown for snapshot ULX2.5-MG. The white contour line corresponds to $F_r/cE_r = 0.3$, which defines the polar funnel angle $\theta_f = 50^\circ$ (with respect to the polar axis). The apparent anisotropy of the gas temperature in the regions above and below the disk is a result of the time this particular simulation was taken. The temperatures were capped at a maximum of 3×10^8 K and a minimum of 10^6 K.

rates in the gray snapshots, these new runs find larger gas temperatures in the regions near or above the photosphere of the accretion flow. Similar to the gray snapshot gas temperatures in Figure 3, the gas temperatures of its multigroup analogue, snapshot ULX2.5-MG, are shown in Figure 10. We

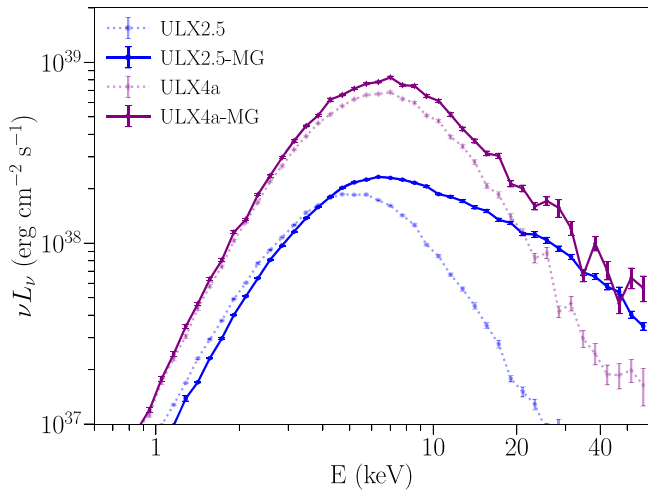


Figure 11. MC postprocessed spectra from the gray RMHD simulation snapshots (ULX2.5 and ULX4a) shown as the lighter blue and purple colored dotted lines, respectively, and the MC spectra from the multigroup RMHD implementation shown as the corresponding darker solid lines. The spectra for ULX2.5 and ULX2.5-MG were computed for a funnel region of $\theta_f = 50^\circ$, while ULX4a and ULX4a-MG were computed for $\theta_f = 37^\circ$.

postprocess these multigroup snapshots following the same procedures as we did for the gray snapshots.

We do not show the angular distributions of the emitted spectra for these multigroup snapshot calculations because they are rather similar to their counterparts shown in Figure 8. We show, however, a second set of reconstructed images in the top panel of Figure 9 for ULX2.5-MG. Compared to its gray counterpart in the top panel, the overall intensities in the multigroup approach are larger due to the larger temperatures, but the mild relativistic beaming again enhances the intensities for off-axis viewing angles relative to those of the most face-on image.

Figure 11 shows the MC postprocessed spectra from the multigroup snapshots compared to their corresponding gray snapshot counterparts. The multigroup approach leads to harder spectra due to the larger gas temperatures. This is seen as both a shift in the spectral peak and a somewhat flatter power-law dependence at higher energies. The effect is larger for ULX2.5-MG than ULX4a-MG. The overall luminosity of the funnel for the multigroup spectra is also larger, with $L_f = 4.73 \times 10^{38} \text{ erg cm}^{-2} \text{ s}^{-1}$ for ULX2.5-MG, and $L_f = 1.31 \times 10^{39} \text{ erg cm}^{-2} \text{ s}^{-1}$ for ULX4a-MG. There is also a commensurate increase in the radiation efficiencies since the accretion rates were essentially unchanged.

Figure 12 shows a comparison of the radiation energy density for ULX2.5-MG from the multigroup RMHD simulation (left panel) and the MC calculated radiation energy density (right panel), analogous to the comparison for the gray snapshot ULX2.5 in left and right panels of Figure 4. As expected, the E_r in the multigroup approach is lower compared to its gray counterpart, and the comparison with MC for the multigroup approach is in closer agreement, although not exact. Exact agreement is not necessarily expected as the Kompaneets treatment in the RMHD module differs slightly from the MC treatment. It is also possible that the (computationally expensive) multigroup calculation has not yet reached full equilibrium.

3.4. Simulated Spectra in Comparison with Phenomenological Models

Here we quantitatively characterize the postprocessed spectra by utilizing X-ray spectral fitting models commonly used to describe observations of black hole sources. The motivation here is to get a sense of how the combinations of phenomenological models describe the hard X-ray emission and quantitatively compare between the postprocessed gray RMHD spectra and the multigroup RMHD spectra. Although we utilize spectral fitting methodology as a tool to compare our simulations to other models, we emphasize that these are not fits to the data, and we make choices in accordance with these considerations.

We use the X-ray spectral fitting package XSPEC (Arnaud 1996) version 6.26.1 to explore a few different model combinations. We note that the two-component (soft + hard) phenomenological model combinations we use here are typically used to fit BHXB spectra while ULX spectra can also be described by two-component models (as shown using variability studies; e.g., Middleton et al. 2015a), where the components refer to regions in the super-Eddington disk, modified by opacity in the wind and anisotropy (Poutanen et al. 2007). In addition, ULX spectra sometimes require a third component at higher energies from a pulsing component (an accretion column; e.g., Brightman et al. 2016; Walton et al. 2018), which has led to speculation that a generic hard excess compared to thermal models could indicate the presence of a highly magnetized neutron star (Pintore et al. 2017; Walton et al. 2018). By comparison, our spectra only correspond to the innermost regions and so miss a large portion of the soft X-ray emission from outer radii; we therefore use only one soft X-ray and one hard X-ray component to describe our simulated spectra, and focus mainly on the hard X-ray part of the spectra. Since we only seek to characterize our simulated spectra, we do not include any absorption components that are typically used to account for the interstellar medium along the line of sight.

The simulated spectra were transcribed into table models containing energies and fluxes that could be loaded into XSPEC. For each simulated model, the energy range was limited to 3–50 keV. We used the `fakeit none` command to generate an artificial “data set” for each simulated table model. For the required response file during this process, we input a NuSTAR FPMA detector response file provided by one of the Gúrpide et al. (2021) observations of NGC 1313 X-1 (see following subsection). All artificial data sets were generated assuming a 100 ks exposure time. The systematic error was set to 5%, a large fraction compared to the error from the counting statistics. The inclusion of a large systematic error is chosen so that this fitting procedure gives a reasonable characterization of the hard X-ray tails in our synthetic spectra. This is, of course, different from standard fitting procedures to data where bins with more counts generally have higher signal-to-noise ratios and are thus weighted more heavily in the fit. The inclusion of a large systematic error results in the bins in the hard X-ray tail being treated on a more equal footing with those near the peak. If not included, the best-fit spectral slopes are notably flatter than our synthetic spectra in the hard X-ray tail. This is due to relatively small changes in the fit near the peak, which drive larger changes to χ^2 than the large deviations in the X-ray tail. The procedure employed here, however, provides a reasonable match to both the continuum near the peak and in the X-ray tail.

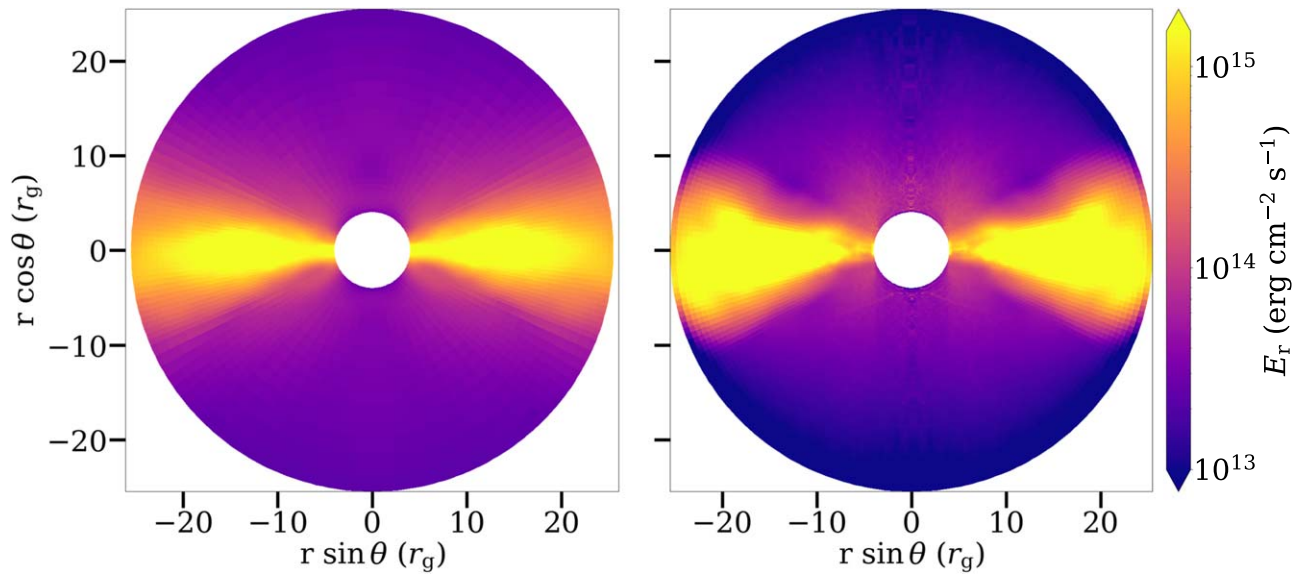


Figure 12. Comparison of the radiation energy density E_r for ULX2.5-MG from the multigroup RMHD snapshot (left panel) and the same quantity calculated by the MC module (right panel). In both cases, the simulation has been azimuthally averaged.

Table 2
Model Comparisons

Model Component	Parameter	ULX2.5	ULX2.5-MG	ULX4a	ULX4a-MG
bbody	kT	1.13	1.42	1.46	1.39
	N_{BB}	0.23	0.32	0.85	0.99
simpl	Γ_{S}	4.38	2.82	4.34	3.52
	f_{sc}	60%	60%	60%	60%
diskbb	T_{in}	1.71	2.27	2.47	2.04
	N_{DBB}	149.92	56.42	116.21	288.64
simpl	Γ_{S}	4.34	2.88	4.14	3.57
	f_{sc}	41.5%	60%	52.2%	60%
diskbb	T_{in}	2.35	4.30	3.06	3.34
	N_{DBB}	25.39	2.07	37.65	23.36
pow	Γ_{P}	3.36	2.40	3.03	2.80

Note. Comparison of commonly used spectral fitting models when fit to the MC postprocessed gray RMHD snapshot spectra (ULX2.5 and ULX4a) and the MC postprocessed multigroup RMHD snapshot spectra (ULX2.5-MG and ULX4a-MG). We only report rough values for each model parameter without errors in an effort to get a sense of the relative spectral shape of the simulated spectra for different model combinations. The accretion disk models used to fit the softer part of the spectrum (diskbb and bbody) were combined with either the Comptonization model simpl or power-law model pow to fit the hard X-ray fluxes.

After the artificial data sets were generated, we chose a sample of model combinations listed in Table 2 along with the corresponding fit parameters. The model bbody fits a blackbody spectrum with two parameters: a temperature kT (keV) and normalization, the latter given by $N_{\text{BB}} = L_{39}/D_{10}^2$, where L_{39} is the source luminosity in units of 10^{39} erg s^{-1} and D_{10} is the distance to the source in units of 10 kpc. Similarly, the diskbb model is a multitemperature blackbody accretion disk (without a color temperature correction factor) and has two free parameters: the inner disk temperature T_{in} (K) and a normalization parameter defined as $N_{\text{DBB}} = (R_{\text{in}}/D_{10})^2 \cos \theta$ where R_{in} is the apparent inner disk radius in kilometers, D_{10} is the distance to the source in units of 10 kpc, and θ is the disk inclination angle at which $\theta=0$ is face on (Mitsuda et al. 1984).

In addition to the accretion disk models, a hard X-ray component was added to characterize the hard X-ray flux. We chose the power-law model pow, which has two free parameters: the power-law index Γ (such that flux goes as

$E^{-\Gamma}$) and a normalization parameter. The other model we chose to characterize the hard X-ray spectrum is the X-ray Comptonization model simpl (Steiner et al. 2009). simpl is a convolution model that approximately Compton up-scatters a fraction f_{sc} of seed photons from the bbody or diskbb models. These up-scattered photons form a hard X-ray power-law tail with index Γ . We assume that photons will only be up-scattered, leaving two free fit parameters, similar to pow. For the model combinations that include simpl, we set an upper limit on the scattering fraction of $f_{\text{sc}} = 60\%$ as this parameter was not well constrained at higher f_{sc} .

We report the fit results in Table 2. We only report a few significant digits without the errors as these are essentially model fits to simulated data, in contrast to model fits to observed data. Any errors computed here would strongly depend on the chosen systematic and stochastic errors, and are not physically meaningful. We do not report goodness of fit for similar reasons.

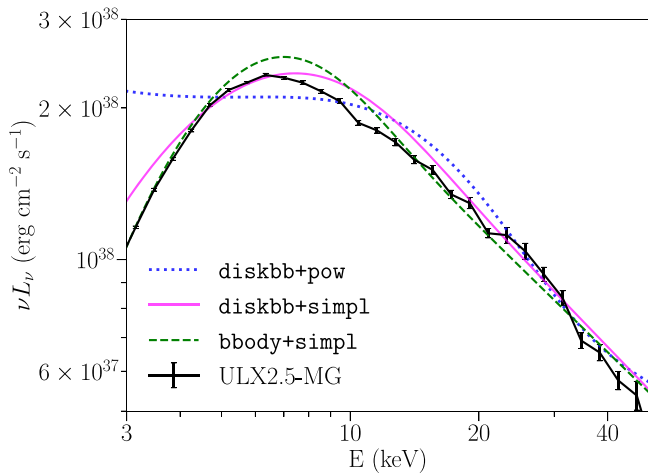


Figure 13. Comparison of three X-ray spectral fitting models to the postprocessed multigroup RMHD spectrum ULX2.5-MG (shown as the black solid line). The model combinations include two components, one blackbody (`bbody`) or multitemperature blackbody accretion disk `diskbb` model paired with either a power law (`pow`) or a hard X-ray Comptonization model (`simpl`). The total combinations are shown as the blue dotted line for `diskbb+pow`, pink solid line for `diskbb+simpl`, and green dashed line for `bbody+simpl`. Note that the `simpl` model in XSPEC would be written as `simpl × diskbb`, since it is a convolution model.

For the gray snapshots, we find a rather steep power-law index of $\Gamma > 4$ is required for all fits when `simpl` is used. The index is still steep, but somewhat flatter when `pow` is used. With the combination of `diskbb+pow`, the `pow` model component dominated the fit and could not adequately describe the softer part of the spectrum. This is partly because we are missing a large portion of the soft X-rays from the outer disk in the simulations, but is also related to the lack of an absorption model to attenuate the power-law emission at softer energies. In contrast, the multigroup snapshots were characterized by much flatter hard X-ray tails (e.g., $\Gamma \lesssim 4$) than their gray counterparts, particularly for ULX2.5-MG ($\Gamma \lesssim 3$). These flatter indices are in better agreement with most observed spectra (Pintore et al. 2017; Dage et al. 2021; Gúrpide et al. 2021). We also generally find high scattering fractions (e.g., $f_{sc} \sim 60\%$) for the multigroup spectra compared to their gray counterparts (e.g., $f_{sc} \sim 40\%–50\%$), particularly for the `diskbb+simpl` model fits. This is indicative of the fact that the power law extends from near the spectral peak.

Figure 13 shows an example of the three model combination fits to ULX2.5-MG. The ULX2.5-MG spectrum is shown as the black solid line. The total `diskbb+pow` model corresponds to the blue dotted line, which shows deviation of the fit at the softer end of the spectrum due to the `pow` component dominating the fit. Interestingly, the `bbody+simpl` model more closely fits the simulated spectra compared to the other two model combinations. For most of the spectra, the `diskbb` component in the `diskbb+simpl` model was slightly broader than the simulated spectrum as seen by the pink solid line in Figure 13. However, this may again be impacted by the missing soft X-rays from larger radii.

3.5. Example Analysis: NGC 1313 X-1

NGC 1313 X-1 is a well known ULX ($L_x \sim 10^{40}$ erg s $^{-1}$) located relatively nearby ($D \sim 4.2$ Mpc; Tully et al. 2013). The nature of its compact accretor is not currently known (Walton et al. 2020), although it has been suggested that changes

observed in its hard X-ray flux might be consistent with a weakly magnetized neutron star (Middleton et al. 2023) entering a propeller state, where any pulsations (when not in propeller) are diluted due to scattering into the wind cone (Mushtukov et al. 2020). Regardless of the nature of its compact object, an interesting feature of this source is the mostly stable shape of the hard X-ray spectrum $E \gtrsim 10$ keV as revealed by NuSTAR observations (Walton et al. 2020); this hard X-ray coverage makes NGC 1313 X-1 an excellent option for trialing our simulated spectral models.

Table 3 shows the best-fit parameters for fits to the combined XMM-Newton and NuSTAR observations of NGC 1313 X-1 (Walton et al. 2020). The data for NGC 1313 X-1 were provided by Gúrpide et al. (2021). For the NuSTAR data we selected energies between 3 and 70 keV, and for the XMM-Newton data we used energies between 0.3 and 10 keV. In all of the fits, we allow two multiplicative constants to vary freely between the XMM-Newton and NuSTAR data sets to account for cross calibration between the different detectors. The FPMA detector constant was set to unity, while the two free constants yielded values $\lesssim 1.38 \pm 0.2$.

We first highlight the “Typical model” column, which includes two modified disk blackbody components and one hard X-ray component that is commonly used to fit this source (Middleton et al. 2015b; Pinto et al. 2016; Walton et al. 2020; Gúrpide et al. 2021). To account for the hydrogen column along the line of sight for all model fits in this analysis, we include a neutral absorption component, `TBabs`, adopting the abundances from Wilms et al. (2000) and cross sections from Verner et al. (1996). The column N_H was left free to vary (see Middleton et al. 2015b; Gúrpide et al. 2021, for some discussion on the variability in the absorption column for this source). The two modified disk blackbody components in this model combination are `diskbb` and `diskpbb`, used to model the softer and harder emission components, respectively. The `diskpbb` component includes a free parameter, p , which describes the radial dependence of the local disk temperature, $T(r) \propto r^{-p}$. When advection in the disk is considered important, such as in the case of super-Eddington accretion, the p -values are typically $p < 0.75$ (Abramowicz et al. 1988). When $p = 0.75$, the model recovers the thin disk `diskbb` solution.

Observations of NGC 1313 X-1 also show emission and absorption lines at energies $E \lesssim 2$ keV that are attributed to the presence of a mildly relativistic disk wind (Middleton et al. 2014, 2015b; Pinto et al. 2016, 2020; Gúrpide et al. 2021). Multiple Gaussian absorption components, `gabs`, are often included to account for some of these atomic features. We limit the `gabs` parameters to $E \leq 2$ keV, line width $\sigma \leq 0.5$ keV, and the line strength was allowed to be positive or negative to represent either emission or absorption. In the Typical model, an additional component at moderate to high energies ($\gtrsim 10$ keV) is included to capture the X-ray excess not adequately modeled by the multitemperature disk components (see Walton et al. 2020). We apply the same `simpl` convolution model to the `diskpbb` component as in previous works. We set a lower limit on the power-law index parameter $\Gamma \geq 2$ as the uncertainties in the data at high energies $E \gtrsim 30$ keV cause `simpl` to return an unrealistically flat power law. The Typical model is written as `TBabs × gabs × (diskbb + (simpl × diskpbb))`. This model provides a reasonably good fit with $\chi^2 = 373.60$ for 341 dof, comparable to the best fits reported in Middleton et al. (2015a),

Table 3
Best-fit Parameters to NGC 1313 X-1 Data Using Simulated Spectral Models

Model Component	Parameter	Typical Model	ULX2.5	ULX2.5-MG	ULX4a	ULX4a-MG
TBabs	n_{H} (cm^{-2})	$0.27^{+0.02}_{-0.03}$	$0.26^{+0.02}_{-0.02}$	$0.16^{+0.03}_{-0.02}$	$0.15^{+0.02}_{-0.02}$	$0.19^{+0.02}_{-0.03}$
diskbb	T_{in} (keV)	$0.27^{+0.03}_{-0.03}$	$0.27^{+0.01}_{-0.01}$	$0.72^{+0.04}_{-0.03}$	$0.68^{+0.03}_{-0.02}$	$0.72^{+0.03}_{-0.03}$
	N_{DBB}	$11.2^{+7.9}_{-4.3}$	$13.83^{+6.9}_{-6.2}$	$0.30^{+0.07}_{-0.07}$	$0.42^{+0.08}_{-0.7}$	$0.33^{+0.06}_{-0.06}$
MC spectrum	N ($\times 10^{-6}$)	n/a	$100.0^{+1.8}_{-1.8}$	$74.2^{+2.1}_{-2.1}$	$26.5^{+0.6}_{-0.7}$	$22.1^{+0.6}_{-0.5}$
diskpbb	T_{in} (keV)	$3.22^{+0.62}_{-0.46}$	n/a	n/a	n/a	n/a
	p	$0.56^{+0.03}_{-0.02}$	n/a	n/a	n/a	n/a
	N_{p} ($\times 10^{-4}$)	$4.49^{+5.6}_{-2.5}$	n/a	n/a	n/a	n/a
simpl	Γ	$2.00^{+0.53}_{-2}$	n/a	n/a	n/a	n/a
	f_{sc} (%)	$11.50^{+7.8}_{-6.1}$	n/a	n/a	n/a	n/a
	χ^2/dof	373.60/341	777.71/345	403.37/345	445.72/345	399.05/342

Note. Best-fit parameter values from the simulated spectral model fits to the combined XMM-Newton and NuSTAR data of NGC 1313 X-1. We also show a comparison “Typical model” fit to NGC 1313 X-1, for comparison to the fits from the four postprocessed or simulated snapshot spectral models. The two models ULX4a-MG and ULX2.5-MG include the multigroup implementation, whereas the other snapshots are postprocessed from the gray RMHD snapshots. The notation “n/a” indicates that this model parameter was not included in the fit and the degrees of freedom (dof) are indicated in the last row.

Walton et al. (2020), and Gúrpide et al. (2021). One difference in our reproduction of this model is that we only included one *gabs* component with line energy $E = 1$ keV, a line width of $\sigma = 0.01$ keV, and line strength $N_{\text{gabs}} = -0.02$. In particular, this differs from the lines modeled in Middleton et al. (2015b), which were found at $E \simeq 0.66\text{--}0.74$ keV and $E \simeq 1.23\text{--}1.46$ keV. If we restricted our model to include these specific lines, the fit returned $\chi^2 = 86.35$ for 338 dof, which is a poorer χ^2 than with a single *gabs* component. The overall fit is qualitatively similar between the two, however we noticed that the f_{sc} went to nearly 0 if we used too many *gabs* components.

To compare to the Typical model, we replaced the `simpl` `diskpbb` component with one of the postprocessed spectral models denoted in XSPEC as `TBabs` \times `gabs` \times (`diskbb` + MC spectrum). The `diskbb` component is included to model the soft X-ray flux absent from our spectral models. The spectral models have one fit parameter, $N = (10 \text{ kpc}/D)^2$, where D is the distance to the source. Assuming the distance to NGC 1313 X-1 is $D = 4.25$ Mpc (Tully et al. 2013) gives an MC spectrum model normalization value of $N = 5.67 \times 10^{-6}$. Table 3 shows the best-fit XSPEC values for four snapshot models: ULX2.5, ULX4a, and their corresponding multigroup runs ULX2.5-MG and ULX4a-MG. We also fit the other two spectral models from ULX1.3 and ULX4b, but for the sake of brevity and the lack of a multigroup counterpart for these snapshots, we do not include them in Tables 2 or 3 but note that they provide poor fits to the data (the best fit for ULX1.3 returned a $\chi^2 = 637.87$ for 345 dof, and ULX4b returned a $\chi^2 = 432.19$ for 345 dof).

All of the spectral model fits included a single *gabs* component except for ULX4a-MG, which included two *gabs* components. Most of the fits were insensitive to a second *gabs* component, but the χ^2 for ULX4a improved from $\chi^2 = 433.20$ per 345 dof with only one Gaussian absorption component to $\chi^2 = 394.50$ per 342 dof with the addition of a second Gaussian component. The two *gabs* components fit lines at 0.34 keV with $\sigma = 0.49$ keV, and a line at 0.67 keV with $\sigma = 0.15$ keV. Generally, modeling the absorption and emission features of this source improves the χ^2 of the fit residuals below 2 keV, but it does not significantly impact the broader continuum fit. Thus we do not attempt to model these features in any detail as past studies have already done (Middleton et al. 2015b; Pinto et al. 2016, 2020; Gúrpide et al. 2021; Kosec et al. 2021).

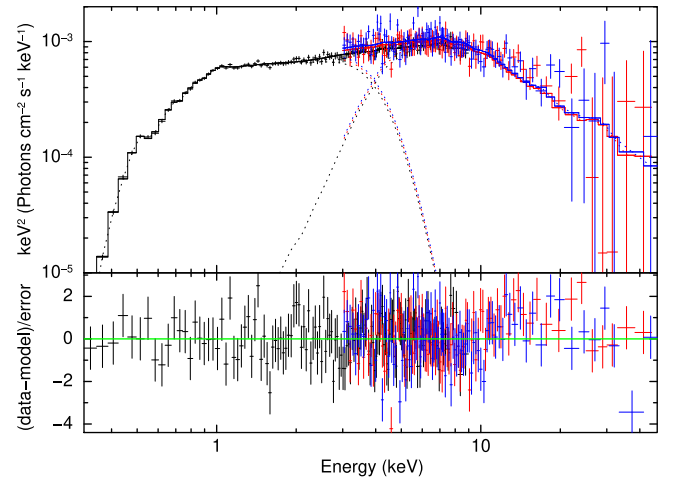


Figure 14. Best fit to the combined XMM-Newton (black data points) and NuSTAR data (red and blue data points) of the ULX NGC 1313 X-1 using the postprocessed spectral model from ULX4a-MG. The top panel shows the spectral fit to the data with individual model components shown for `diskbb` (below 10 keV) and the ULX4a-MG model fitting the rest of the hard X-ray spectrum. The bottom panel shows the fit residuals of the total model (green line) to the data. The best-fit values are collected in Table 3.

The $\Delta\chi^2$ improves significantly for fits with the multigroup models, as the harder X-ray tails in the models better match the observed NuSTAR data.

We show the two multigroup model combinations in Figures 14 and 15 for ULX4a-MG and ULX2.5-MG, respectively. The individual model components are shown for the absorbed `diskbb` component below 10 keV and the component modeling the higher energy flux. ULX4a-MG in Figure 14 is just slightly steeper than the NuSTAR data at $\gtrsim 10$ keV, while ULX2.5-MG in Figure 15 is just slightly flatter at $\gtrsim 10$ keV. Both spectral models, however, fit quite well in the 3–10 keV range. Considering the simulated spectral component only has one parameter (the normalization), the deviation of the fit at $E \gtrsim 10$ keV qualitatively seems fairly reasonable.

4. Discussion

Our results suggest that RMHD simulations can qualitatively reproduce the observed hard X-ray spectral shape seen in a

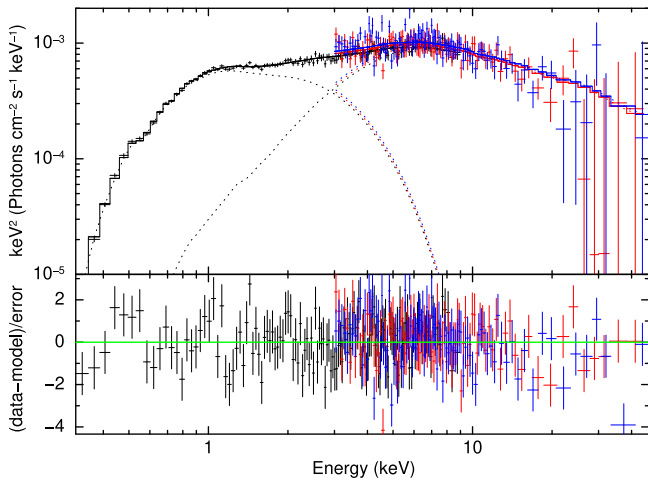


Figure 15. Same as Figure 14, but using the ULX2.5-MG spectral model to fit the hard X-ray spectrum.

number of ULX sources as long as the radiative heating/cooling associated with Compton scattering processes are well modeled. Nevertheless, the simulations presented here have only explored a limited range of parameter space and do not yet include all of the relevant physics. Most importantly, the Athena++ RMHD simulations neglect general relativistic effects such as light bending, relativistic beaming, and relativistic jets (although these simulations do generate radiatively driven disk winds). New GRRMHD simulations are being performed with Athena++ using the direct solutions of the radiation transfer equations (White et al. 2023) and we expect that the inclusion of general relativistic effects will have an impact on the accretion flow, disk structure, and associated spectral properties. Postprocessed spectra from such GRRMHD simulations will be the focus of future work.

In addition, we only include the inner $25 r_g$ of these RMHD simulations in our MC spectral calculations as the simulation is not in steady state at larger radii. Thus, we do not accurately model the soft X-ray flux originating beyond $25 r_g$. Consequently, we only select photons coming out of a polar funnel angle, θ_f to avoid the impact of photons which would normally interact with outer disk radii and become trapped in the disk or advected into the black hole. Therefore, we stress that interpretations of these results be limited to the inner regions of the flow.

We also assume that protons and electrons are well coupled and so simulate a single temperature accretion flow $T = 10^7$ K. Some studies have suggested that two-temperature accretion flows may become important in areas of low density, such as in the funnel regions (Liska et al. 2022) and may result in softer X-ray spectra (Kinch et al. 2020). We compared the nonrelativistic proton–electron relaxation timescale given by Spitzer (1956) and Stepney (1983) assuming a single temperature for both the electrons and protons with the Compton timescale $t_C = (N_e \sigma_T c)^{-1}$ where N_e is the number density of electrons, σ_T is the Thomson cross section, and c is the speed of light. We found that the relaxation time is much shorter than the Compton timescale and most other dynamical timescales for the temperature and densities in our simulation, except possibly in the very low-density, high-temperature region near the axis. Hence, our assumption of a single temperature for the protons and electrons seems self-consistent,

but the single temperature assumption may need to be revisited in future work, particularly for simulations at lower accretion rates.

4.1. Comparison with NGC 1313 X-1

Fits to the XMM-Newton and NuSTAR data of NGC 1313 X-1 with the postprocessed spectral models qualitatively reproduce the hard X-ray part of the spectrum, although the funnel luminosities for these spectra are at least an order of magnitude lower ($L_f = 1.3 \times 10^{39}$ erg s $^{-1}$ for ULX4a-MG, and $L_f = 4.7 \times 10^{38}$ erg s $^{-1}$ for ULX2.5-MG) than the observed luminosity ($L_x \sim 10^{40}$ erg s $^{-1}$). The implied distances from the spectral models are also much smaller ($D \sim 1\text{--}2.13$ Mpc) when compared to the true distance to NGC 1313 X-1 of $D \simeq 4.25$ Mpc (Tully et al. 2013). This motivates future work with simulations at higher Eddington ratios and across a range of black hole masses, which might then better match the observed sources at their known distances. Nevertheless, it is remarkable that a first principles calculation with only the normalization as a free parameter can provide best-fitting χ^2 values that are quantitatively competitive with commonly used phenomenological models.

4.2. Comparison with Previous Work

Previous simulations have explored a range of accretion rates and masses, using a variety of setups both with and without general relativistic effects, finding radiative efficiencies that are both relatively large ($\eta \sim 5\%$; e.g., Jiang et al. 2014) or small ($\eta \lesssim 1\%$; e.g., Sądowski et al. 2014). The radiative efficiencies inferred directly from the gray RMHD simulations are typically a few percent, somewhat less than expected for thin accretion disks but not inconsistent with expectations for modestly super-Eddington accretion rates. The radiative efficiencies $\eta_f = 1.13\% \text{--} 2.56\%$ for the funnel region computed with MC postprocessing are modestly lower than from the RMHD simulations for the gray snapshots. In contrast, the snapshots produced from the multigroup calculations have slightly larger efficiencies ($\eta_f = 1.92\%$ for ULX2.5-MG and $\eta_f = 3.34\%$ for ULX4a-MG), in better agreement with the luminosities directly inferred from RMHD simulations.

The MC radiation transfer calculations performed in this work are similar to other postprocessing codes, particularly those that use MC methods (Dolence et al. 2009; Schnittman et al. 2013; Kawashima et al. 2023) that model Compton scattering and include general relativistic effects. The HEROIC code (Narayan et al. 2017), which uses a combination of short and long characteristics instead of MC, provides similar capabilities. Although the Athena++ module used here also supports general relativistic transfer, we treat the radiation transfer in Minkowski spacetime to be consistent with the nonrelativistic simulations that generate the snapshots. In contrast to Kinch et al. (2019), we do not currently perform any ionization calculations that would investigate atomic transitions. We also do not use any integrated ray tracing algorithms that would integrate back along the photon path in our postprocessing; although to create the images in Figure 9, we extrapolate the photons escaping the MC domain out to a distant observer assuming flat spacetime.

Our approach compares most directly to those of Narayan et al. (2017) and Kitaki et al. (2017), who consider the spectra produced from super-Eddington accretion simulations. Our results are broadly consistent with those of Kitaki et al. (2017),

at least when one focuses on the hard component of the spectrum and face-on inclinations for the $10 M_{\odot}$ black hole simulations. Narayan et al. (2017) used HEROIC to postprocess simulations from the GRRMHD code KORAL (Sądowski et al. 2013, 2014; Sądowski & Narayan 2015, 2016), which was used to simulate a broad range of super-Eddington accretion rates onto a $10 M_{\odot}$ black hole. They faced the same issue in that their GRRMHD simulations only reached inflow equilibrium out to a finite radius. Instead of truncating the disk as we chose to do, they instead extrapolated the flow to larger radii using self-similar approximations. This allowed them to explore the softer X-ray emission and angular dependence, but with the caveat that the outer regions of the calculation were not simulated directly. We find that our spectra are more qualitatively consistent with their results when the gas temperatures in the HEROIC calculation were fixed to the values from KORAL (see the green curves in Figure 4 of Narayan et al. 2017), but not consistent with their spectra after the radiation field and temperatures were self-consistently solved (red curves in the same figure). The results from HEROIC show that their spectra become much softer after the temperature iteration, while our results suggest that a more self-consistent treatment of Compton cooling yields higher temperatures and harder spectra. The origin of the difference is not clear to us, but we note that the KORAL simulations use a photon number conservation scheme that is different from what we use in our gray simulations.

5. Summary

We present MC postprocessed spectral calculations of super-Eddington accretion onto a stellar-mass black hole from the Athena++ RMHD simulation snapshots. Our calculations suffer from two primary deficiencies. We only achieve inflow equilibrium out to $\sim 25 r_g$, which led us to truncate our spectral calculations at this radius. Hence, the soft X-rays that come from the outer disk are absent. If we instead include emission from the outer disk, it is significantly overestimated due to the cooling of the torus. Therefore we mainly focus on the hard X-ray spectrum in this work. These simulations also assume that the intensities follow a blackbody spectrum for the purposes of computing Compton cooling and mean opacities. Although this assumption is good for the optically thick disk, we find that using the blackbody assumption to estimate the average photon energy in the Compton cooling term is a poor approximation in the funnel regions where Comptonized electrons dominate the cooling. This leads to an underestimate of the temperatures in the funnel for the gray RMHD simulations. The underestimated temperatures produced spectra that were much softer and led to radiation energy densities above the disk being overestimated. We addressed this underestimate of the temperature by restarting the gray opacity simulations with a multigroup approach (Jiang 2022) that treats Compton scattering with a Kompaneets-like source term. This produced simulation snapshots with higher temperatures in the spectral forming regions above the disk, leading to harder X-ray flux in better agreement with observed ULX spectra.

We used phenomenological models to fit our MC spectra. In most of the two-component (soft X-ray and hard X-ray) models, the hard X-ray component was more accurately described with the SIMPL model compared to the power-law POW model, and yielded hard X-ray power-law slopes ranging from $\Gamma \sim 2-4$ for spectra computed with gray RMHD



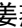

snapshots. The multigroup snapshot spectra tended to be fitted with flatter slopes, with $\Gamma \sim 2-3$, comparable to the hard X-ray tails observed in NGC 1313 X-1 and Holmberg IX X-1 (Gürpide et al. 2021).

Finally, we generated an XSPEC table model and directly fit our MC spectra to combined XMM-Newton and NuSTAR observations of the ULX NGC 1313 X-1. Despite only having one free parameter (the normalization), we find a good fit, which is competitive with the phenomenological models that are commonly used. Close inspection shows that the MC spectra provide a good fit at soft to moderately hard energies of $E \lesssim 10$ keV, but are either just slightly too steep in the case of ULX4a-MG or too flat in the case of ULX2.5-MG to exactly describe the hard X-ray power-law tail at $E \gtrsim 10$ keV. The best-fit normalizations are also not consistent with the known distance to NGC 1313 X-1 and the model implies a lower luminosity than is observed. Although there are a number of caveats (such as the absence of general relativistic effects) and we have used only a single black hole mass and a relatively narrow range of accretion rates, this work nonetheless provides a promising direction for super-Eddington ULX accretion simulations, as these postprocessed spectral models are close to describing the observed spectrum of NGC 1313 X-1. Simulations with the new GRRMHD implementation of the Athena++ code (White et al. 2023) are now exploring a range of masses and accretion rates, and postprocessed spectra from these simulation will be presented in a future work.

Acknowledgments

This work was supported by NASA TCAN grant 80NSSC21K0496 and NASA ATP grant 80NSSC18K1018. B.S.M. thanks the Jefferson Scholars Foundation Graduate Fellowship in support of this work. This work used the computational resources provided by Research Computing at the University of Virginia. Part of this work was performed using resources provided by the Cambridge Service for Data Driven Discovery (CSD3) operated by the University of Cambridge Research Computing Service (www.csd3.cam.ac.uk), provided by Dell EMC and Intel using Tier-2 funding from the Engineering and Physical Sciences Research Council (capital grant EP/T022159/1), and DiRAC funding from the Science and Technology Facilities Council (www.dirac.ac.uk). Resources supporting this work were also provided by the High-End Computing (HEC) program through the NASA Advanced Supercomputing (NAS) Division at Ames Research Center. The Center for Computational Astrophysics at the Flatiron Institute is supported by the Simons Foundation.

ORCID iDs

Brianna S. Mills  <https://orcid.org/0000-0003-0148-2817>
 Shane W. Davis  <https://orcid.org/0000-0001-7488-4468>
 Yan-Fei Jiang (姜燕飞)  <https://orcid.org/0000-0002-2624-3399>
 Matthew J. Middleton  <https://orcid.org/0000-0002-8183-2970>

References

- Abramowicz, M. A., Czerny, B., Lasota, J. P., & Szuszkiewicz, E. 1988, *ApJ*, 332, 646
- Arnaud, K. A. 1996, in ASP Conf. Ser. 101, *Astronomical Data Analysis Software and Systems V*, ed. G. H. Jacoby & J. Barnes (San Francisco, CA: ASP), 17

- Asahina, Y., Takahashi, H. R., & Ohsuga, K. 2020, *ApJ*, 901, 96
- Bachetti, M., Harrison, F. A., Walton, D. J., et al. 2014, *Natur*, 514, 202
- Balbus, S. A., & Hawley, J. F. 1991, *ApJ*, 376, 214
- Brightman, M., Harrison, F. A., Barret, D., et al. 2016, *ApJ*, 829, 28
- Chandrasekhar, S. 1960, *Radiative Transfer* (New York: Dover)
- Dage, K. C., Vowell, N., Thygesen, E., et al. 2021, *MNRAS*, 508, 4008
- Davis, S. W., Blaes, O. M., Hirose, S., & Krolik, J. H. 2009, *ApJ*, 703, 569
- Davis, S. W., Stone, J. M., & Jiang, Y.-F. 2012, *ApJS*, 199, 9
- Dolence, J. C., Gammie, C. F., Mościbrodzka, M., & Leung, P. K. 2009, *ApJS*, 184, 387
- Earnshaw, H. M. 2016, *AN*, 337, 448
- Event Horizon Telescope Collaboration, Akiyama, K., Alberdi, A., et al. 2019, *ApJL*, 875, L5
- Event Horizon Telescope Collaboration, Akiyama, K., Alberdi, A., et al. 2022, *ApJL*, 930, L16
- Farrell, S. A., Webb, N. A., Barret, D., Godet, O., & Rodrigues, J. M. 2009, *Natur*, 460, 73
- Fragile, P. C., Olejar, A., & Anninos, P. 2014, *ApJ*, 796, 22
- Gladstone, J. C., Roberts, T. P., & Done, C. 2009, *MNRAS*, 397, 1836
- González, M., Audit, E., & Huynh, P. 2007, *A&A*, 464, 429
- Gürpide, A., Godet, O., Koliopanos, F., Webb, N., & Olive, J. F. 2021, *A&A*, 649, A104
- Howell, L. H., & Greenough, J. A. 2003, *JCoPh*, 184, 53
- Huang, J., Jiang, Y.-F., Feng, H., et al. 2023, *ApJ*, 945, 57
- Jiang, Y.-F. 2021, *ApJS*, 253, 49
- Jiang, Y.-F. 2022, *ApJS*, 263, 4
- Jiang, Y. F., Stone, J. M., & Davis, S. W. 2013, *ApJ*, 767, 148
- Jiang, Y.-F., Stone, J. M., & Davis, S. W. 2014, *ApJ*, 796, 106
- Jiang, Y.-F., Stone, J. M., & Davis, S. W. 2019, *ApJ*, 880, 67
- Kawashima, T., Ohsuga, K., Mineshige, S., et al. 2012, *ApJ*, 752, 18
- Kawashima, T., Ohsuga, K., & Takahashi, H. R. 2023, *ApJ*, 949, 30
- Kinch, B. E., Noble, S. C., Schnittman, J. D., & Krolik, J. H. 2020, *ApJ*, 904, 117
- Kinch, B. E., Schnittman, J. D., Kallman, T. R., & Krolik, J. H. 2019, *ApJ*, 873, 71
- Kinch, B. E., Schnittman, J. D., Noble, S. C., Kallman, T. R., & Krolik, J. H. 2021, *ApJ*, 922, 270
- King, A., Lasota, J.-P., & Middleton, M. 2023, *NewAR*, 96, 101672
- Kitaki, T., Mineshige, S., Ohsuga, K., & Kawashima, T. 2017, *PASJ*, 69, 92
- Kosec, P., Pinto, C., Reynolds, C. S., et al. 2021, *MNRAS*, 508, 3569
- Krumholz, M. R., Klein, R. I., McKee, C. F., & Bolstad, J. 2007, *ApJ*, 667, 626
- Kubota, A., & Done, C. 2019, *MNRAS*, 489, 524
- Levermore, C. D. 1984, *JQSRT*, 31, 149
- Liska, M. T. P., Musoke, G., Tchekhovskoy, A., Porth, O., & Beloborodov, A. M. 2022, *ApJL*, 935, L1
- McKinney, J. C., Tchekhovskoy, A., Sądowski, A., & Narayan, R. 2014, *MNRAS*, 441, 3177
- Menon, S. H., Federrath, C., Krumholz, M. R., et al. 2022, *MNRAS*, 512, 401
- Mezcua, M., Roberts, T. P., Sutton, A. D., & Lobanov, A. P. 2013, *MNRAS*, 436, 3128
- Middleton, M., Gürpide, A., & Walton, D. J. 2023, *MNRAS*, 519, 2224
- Middleton, M. J., Heil, L., Pintore, F., Walton, D. J., & Roberts, T. P. 2015a, *MNRAS*, 447, 3243
- Middleton, M. J., Walton, D. J., Fabian, A., et al. 2015b, *MNRAS*, 454, 3134
- Middleton, M. J., Walton, D. J., Roberts, T. P., & Heil, L. 2014, *MNRAS*, 438, L51
- Miller, J. M., Fabian, A. C., & Miller, M. C. 2004, *ApJL*, 614, L117
- Mitsuda, K., Inoue, H., Koyama, K., et al. 1984, *PASJ*, 36, 741
- Moens, N., Sundqvist, J. O., El Mellah, I., et al. 2022, *A&A*, 657, A81
- Mushtukov, A. A., Portegies Zwart, S., Tsygankov, S. S., Nagirner, D. I., & Poutanen, J. 2020, *MNRAS*, 501, 2424
- Narayan, R., Sądowski, A., & Soria, R. 2017, *MNRAS*, 469, 2997
- Ohsuga, K., & Mineshige, S. 2011, *ApJ*, 736, 2
- Ohsuga, K., Mori, M., Nakamoto, T., & Mineshige, S. 2005, *ApJ*, 628, 368
- Oskinova, L. M., Bik, A., Mas-Hesse, J. M., et al. 2019, *A&A*, 627, A63
- Paczynsky, B., & Wiita, P. J. 1980, *A&A*, 88, 23
- Pinto, C., Middleton, M. J., & Fabian, A. C. 2016, *Natur*, 533, 64
- Pinto, C., & Walton, D. J. 2023, arXiv:2302.00006
- Pinto, C., Walton, D. J., Kara, E., et al. 2020, *MNRAS*, 492, 4646
- Pintore, F., Zampieri, L., Stella, L., et al. 2017, *ApJ*, 836, 113
- Poutanen, J., Lipunova, G., Fabrika, S., Butkevich, A. G., & Abolmasov, P. 2007, *MNRAS*, 377, 1187
- Pozdnyakov, L. A., Sobol, I. M., & Syunyaev, R. A. 1983, *ASPRv*, 2, 189
- Rybicki, G. B., & Lightman, A. P. 1979, *Radiative Processes in Astrophysics* (New York: Wiley-Interscience)
- Schnittman, J. D., Krolik, J. H., & Noble, S. C. 2013, *ApJ*, 769, 156
- Shakura, N. I., & Sunyaev, R. A. 1973, *A&A*, 500, 33
- Sądowski, A., & Narayan, R. 2016, *MNRAS*, 456, 3929
- Sądowski, A., Narayan, R., Tchekhovskoy, A., & Zhu, Y. 2013, *MNRAS*, 429, 3533
- Sądowski, A., Narayan, R., Tchekhovskoy, A., et al. 2015, *MNRAS*, 447, 49
- Skinner, G. K., Bedford, D. K., Elsner, R. F., et al. 1982, *Natur*, 297, 568
- Skinner, M. A., & Ostriker, E. C. 2013, *ApJS*, 206, 21
- Socrates, A., & Davis, S. W. 2006, *ApJ*, 651, 1049
- Spitzer, L. 1956, *Physics of Fully Ionized Gases* (New York: Interscience)
- Steiner, J. F., Narayan, R., McClintock, J. E., & Ebisawa, K. 2009, *PASP*, 121, 1279
- Stepney, S. 1983, *MNRAS*, 202, 467
- Stone, J. M., Gardiner, T. A., Teuben, P., Hawley, J. F., & Simon, J. B. 2008, *ApJS*, 178, 137
- Stone, J. M., Mihalas, D., & Norman, M. L. 1992, *ApJS*, 80, 819
- Stone, J. M., Tomida, K., White, C. J., & Felker, K. G. 2020, *ApJS*, 249, 4
- Straub, O., Bursa, M., Sądowski, A., et al. 2011, *A&A*, 533, A67
- Sądowski, A., & Narayan, R. 2015, *MNRAS*, 453, 3213
- Sądowski, A., Narayan, R., McKinney, J. C., & Tchekhovskoy, A. 2014, *MNRAS*, 439, 503
- Tully, R. B., Courtois, H. M., Dolphin, A. E., et al. 2013, *AJ*, 146, 86
- Turner, N. J., & Stone, J. M. 2001, *ApJS*, 135, 95
- Verner, D. A., Ferland, G. J., Korista, K. T., & Yakovlev, D. G. 1996, *ApJ*, 465, 487
- Walton, D. J., Fürst, F., Heida, M., et al. 2018, *ApJ*, 856, 128
- Walton, D. J., Middleton, M. J., Pinto, C., et al. 2016, *ApJL*, 826, L26
- Walton, D. J., Pinto, C., Nowak, M., et al. 2020, *MNRAS*, 494, 6012
- Webb, N. A., Guérou, A., Ciambur, B., et al. 2017, *A&A*, 602, A103
- White, C. J., Mullen, P. D., Jiang, Y.-F., et al. 2023, *ApJ*, 949, 29
- White, C. J., Stone, J. M., & Gammie, C. F. 2016, *ApJS*, 225, 22
- Wibking, B. D., & Krumholz, M. R. 2022, *MNRAS*, 512, 1430
- Wilms, J., Allen, A., & McCray, R. 2000, *ApJ*, 542, 914
- Zhu, Y., Davis, S. W., Narayan, R., et al. 2012, *MNRAS*, 424, 2504